

Determining the Physical Conditions of an Extremely Young Class 0 Circumbinary Disk around VLA 1623A

Cheng-Han Hsieh^{1,2}, Shih-Ping Lai^{1,3,4}, Pou-Ieng Cheong³, Chia-Lin Ko^{3,5}, Zhi-Yun Li⁶, and Nadia M. Murillo⁷

Department of Physics, National Tsing Hua University, 101 Section 2 Kuang Fu Road, 30013 Hsinchu, Taiwan; cheng-han.hsieh@yale.edu

Department of Astronomy, Yale University, New Haven, CT 06511, USA

Institute for Astronomy, National Tsing Hua University,101 Section 2 Kuang Fu Road, 30013 Hsinchu, Taiwan

Academia Sinica Institute of Astronomy and Astrophysics, P.O. Box 23-141, 10617 Taipei, Taiwan

Department of Physics, National Taiwan Normal University, No. 162, Section 1, Heping East Road, Taipei 10610, Taiwan

Department of Astronomy, University of Virginia, 530 McCormick Road, Charlottesville, VA, USA

Leiden Observatory, Leiden University, P.O. Box 9513, 2300 RA Leiden, The Netherlands

Received 2019 March 29; revised 2020 February 26; accepted 2020 February 27; published 2020 April 30

Abstract

We present a detailed analysis of high-resolution $C^{18}O$ (2–1), SO (8₈–7₇), CO (3–2), and DCO⁺ (3–2) data obtained by the Atacama Large Millimeter/submillimeter Array toward a class 0 Keplerian circumbinary disk around VLA 1623A, which represents one of the most complete analyses toward a class 0 source. From the dendrogram analysis, we identified several accretion flows feeding the circumbinary disk in a highly anisotropic manner. Stream-like SO emission around the circumbinary disk reveals the complicated shocks caused by the interactions between the disk, accretion flows, and outflows. A wall-like structure is discovered south of VLA 1623B. The discovery of two outflow cavity walls at the same position traveling at different velocities suggests that the two outflows from both VLA 1623A and VLA 1623B are on top of each other in the plane of the sky. Our detailed flat and flared disk modeling shows that Cycle 2 $C^{18}O$ J = 2–1 data are inconsistent with the combined binary mass of $0.2 M_{\odot}$, as suggested by early Cycle 0 studies. The combined binary mass for VLA 1623A should be modified to 0.3– $0.5 M_{\odot}$.

Unified Astronomy Thesaurus concepts: Shocks (2086); Accretion (14); Stellar accretion (1578); Stellar accretion disks (1579); Observational astronomy (1145); Protostars (1302); Young stellar objects (1834); Radio interferometry (1346); Radio astronomy (1338); Circumstellar disks (235); Star formation (1569)

1. Introduction

Around 50% of solar mass stars form in multiple systems (Raghavan et al. 2010). The multiplicity fraction increases for higher-mass stars (Sana & Evans 2011). These multiple systems are formed in the early stage of star formation via three processes: turbulent fragmentation, thermal fragmentation of rotating cores, and disk fragmentation. Turbulent and thermal fragmentation occurs at relatively large scales, forming wide binaries with separations of order 1000 au or larger (Inutsuka & Miyama 1992; Burkert & Bodenheimer 1993; Padoan & Nordlund 2002; Offner et al. 2010; Boss & Keiser 2014; Pineda et al. 2015). As for the disk fragmentation, it is believed to be one of the primary processes for forming close (~100 au) binaries (Takakuwa et al. 2012; Tobin et al. 2013).

Previous observations have found many circumbinary disks (Takakuwa et al. 2012; Tobin et al. 2013; Chou et al. 2014; Dutrey et al. 2014, 2016; Tang et al. 2014, 2016). Near-infrared surveys of class I sources have found that around 15 out of 88 targets have binary separations between 50 and 200 au (Duchêne et al. 2007; Connelley et al. 2008). Very Large Array (VLA) surveys of 94 known protostars in the Perseus molecular clouds have found that class 0 sources have a significantly higher multiplicity fraction (MF = 0.57 ± 0.09) as compared to class I sources (MF = 0.23 ± 0.08 ; Tobin et al. 2016). Submillimeter Array studies of 33 class 0 protostars in the nearby molecular clouds also found the multiplicity fraction (MF = 0.64 ± 0.08) to be two times larger than that of the class I sources (Chen et al. 2013). Since disk fragmentation requires massive gravitationally unstable disks, close binary and multiplicity systems are expected to form in the early phase of star formation. Thus,

understanding the gas dynamics in extremely young class 0 protobinary disks is crucial for testing binary formation theory.

Disk formation in the class 0 phase attracted a lot of attention over the last 10 yr, and it remains an important unsolved problem for star formation. Numerical models simulating the collapse of a magnetized envelope with the assumption of ideal magnetohydrodynamics (MHD) show that disk formation is hindered by magnetic braking effects (Mellon & Li 2008). One solution proposed is that magnetic braking efficiency can be reduced if the rotation axis is misaligned with the magnetic field direction (Hennebelle & Ciardi 2009). Moreover, nonideal MHD effects on disk formation have also been explored. Recently, 3D nonideal MHD simulations have been carried out, and a disk around 5 au is formed at the end of the first core phase (Tomida et al. 2015). In the recent analytical study carried out by Hennebelle et al. (2016), a relationship between the disk radius and magnetic fields in the inner part of the core is found. The weak dependence of various relevant quantities suggests that class 0 disks have a typical disk size of \sim 18 au (Hennebelle et al. 2016).

An alternative solution to magnetic braking effects is turbulence. Santos-Lima et al. (2012, 2013) suggested that turbulence reconnection in disks is associated with the loss of magnetic flux, which reduces the magnetic braking efficiency. In contrast, Seifried et al. (2015) showed that even with mild subsonic turbulence motion together with disorder magnetic field is enough for the formation of class 0 Keplerian disks without the need for the loss of magnetic flux. In their simulations, they found that both the accretion of mass and angular momentum are highly anisotropic.

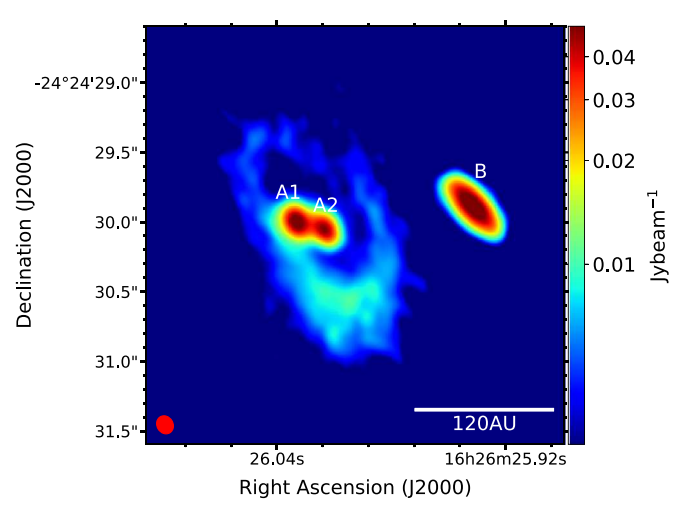


Figure 1. The VLA 1623 0.88 mm continuum image. The class 0 source, VLA 1623A, is resolved into two sources, VLA 1623A1 and VLA 1623A2. The red ellipse marks the beam size.

Numerical simulations tend to have difficulties in explaining how the observed large class 0 disks grow in size and possibly fragment. A well-studied class 0 candidate, HH 212 is found to have a Keplerian disk within the 44 au centrifugal barrier (Lee et al. 2017). The Keplerian disk of class 0 protostar L1527 has a disk radius of 74 au, and the scale height at 100 au is 48 au (Tobin et al. 2013; Aso et al. 2017). As for VLA 1623A, the Keplerian rotating disk size is fitted to 150 au using C¹⁸O as a tracer (Murillo et al. 2013). These observational results show class 0 disks with varying disk sizes and structures. The discovery of large (>70 au) class 0 rotationally supported disks, L1527 and VLA 1623A, provide possible candidates to study disk fragmentation around class 0 sources. Not much is known about how large rotationally supported disks are formed and what factors influence their formation.

Located 120 \pm 4.5 pc away in cloud ρ Ophiuchus A (Andre et al. 1993; Loinard et al. 2008; Ortiz-León et al. 2017), VLA 1623-2417 (hereafter VLA 1623) is a triple noncoeval protostellar system. 8 The system consists of three components: VLA 1623A (class 0 source), VLA 1623B (younger than VLA 1623A and possibly a transition between starless core and class 0; Santangelo et al. 2015), and VLA 1623W (class 1; Murillo & Lai 2013). Recent high angular resolution (\sim 0."16) 0.88 mm continuum data reveal that VLA 1623A is in fact a binary, denoted as VLA 1623A1 and VLA 1623A2 in Figure 1, and the Keplerian disk previously discovered is a circumbinary disk (Harris et al. 2018). The plane-of-sky separation between VLA 1623A1 and VLA 1623A2⁹ is around 0."2, which corresponds to a physical scale of 24 au. Unfortunately, our Cycle 2 C¹⁸O (J = 2-1) data with beam size 0."5 cannot resolve the two sources ($C^{18}O$ moment maps shown in Figure 2).

With the increase of antennas and UV coverage, the Cycle 2 data pick up significantly more $C^{18}O$ emission than the Cycle 0 observations shown in Figure 3. As one of the youngest protobinary disks ever discovered, VLA 1623A is the perfect candidate to study disk fragmentation around class 0 sources.

In what follows, in Section 2 we discuss the data used in this analysis. In Section 3.1 we compare Cycle 0 and Cycle 2 C¹⁸O data and highlight the major emission components that will be further explored. In Section 3 we present the main results of our large-scale emission fitting, dendrogram analysis (P.-I. Cheong et al. 2020, in preparation), flat and flared disk modeling, and accretion shock analysis. In Section 4, we summarize the physical conditions of the VLA 1623A circumbinary disk and its surrounding environment. In Section 5, we give our conclusions.

2. Observations

2.1. CO

We observed the CO (J = 3-2) emission with the Atacama Large Millimeter/submillimeter Array (ALMA) in Cycle 6 with pointing coordinates $\alpha(J2000) = 16^{h}26^{m}26^{s}390$, δ $(J2000) = -24^{\circ}24'30''688$. The observation was taken on 2019 March 15 using 47 antennas of the 12 m array in the C34-1 compact configuration (project ID: 2018.1.00388S; PI: Chenghan Hsieh). The total on-source integration time is 10 minutes sampling baseline ranges between 15.1 and 360.6 m. The ALMA pipeline and Common Astronomy Software Applications (CASA) version 5.4.0-70 are used to calibrate the visibility data with J1924+2914 as the calibrator for bandpass and flux calibration and J1625+2527 for phase calibration. We used the CASA CLEAN task with Briggs 0.5 weighting and Hogbom as the deconvolver for imaging. The resulting image has a beam size of 0.99×0.59 (P.A. = $-84^{\circ}8$) with an rms noise level at 11 mJy beam⁻¹ and a velocity resolution at 0.0529 km s⁻¹.

$2.2. C^{18}O$

ALMA in Cycle 2 with the 12 m array configurations C34-5 and C34-1 (project ID: 2013.1.01004.S; PI: Shih-Ping Lai) observed $C^{18}O$ (J=2-1). We also include the 7 m Atacama Compact Array (ACA; hereafter 7 m array) and Total Power Array of ACA in our analysis. The 12 and 7 m array data are combined via the CASA task CLEAN with a weighting parameter of Briggs -1.5, Briggs -1.0, and a natural weighting. These maps are used for identifying accretion flows, comparing with ALMA $C^{18}O$ Cycle 0 data and analysis of disk motion, respectively.

For the Briggs -1.5 weighting, the UV taper range is 0.25. The resulting $C^{18}O$ (J=2-1) channel map has a resolution of 1.1×0.89 (P.A. = 36.8) with an rms noise level of 18 mJy beam⁻¹. The velocity resolution is 0.0208 km s⁻¹ with a rest frequency of 219.56036 GHz (corresponding to a system velocity of 4.0 km s⁻¹ away in the line of sight). The low-resolution data are used for the dendrogram analysis and for identifying large structures around the circumbinary disk VLA 1623A.

For the natural weighted data, the Hogbom algorithm is used for the deconvolution process, resulting in a resolution of 0."52 \times 0."31 (P.A. = 87.89) with an rms noise level of 9 mJy beam $^{-1}$. The velocity resolution of 0.0832 km s $^{-1}$ is used to achieve a higher signal-to-noise ratio for disk modeling.

For comparison purposes, Briggs -1.0 weighting with a UV taper range of 0."25 is applied to the Cycle 2 C¹⁸O data to achieve a resolution of 0."51 \times 0."31 (P.A. = 61.83) with an rms noise level of 14 mJy beam⁻¹. The velocity resolution is 0.0208 km s⁻¹. This data set is used to compare with the Cycle 0 observation in Figure 3.

⁸ In this paper, a distance of 120 pc (Murillo & Lai 2013) is used in the modeling instead of 137.3 pc (Ortiz-León et al. 2017). The physical scale will increase by a factor of 1.14 if the 137.3 pc distance is adopted.

The nomenclature used in Harris+2018 is VLA 1623Aa and VLA 1623Ab. However, lowercase letters after a source name are reserved for planets. The IAU-stipulated convention for stars should be VLA 1623A1 and VLA 1623A2.

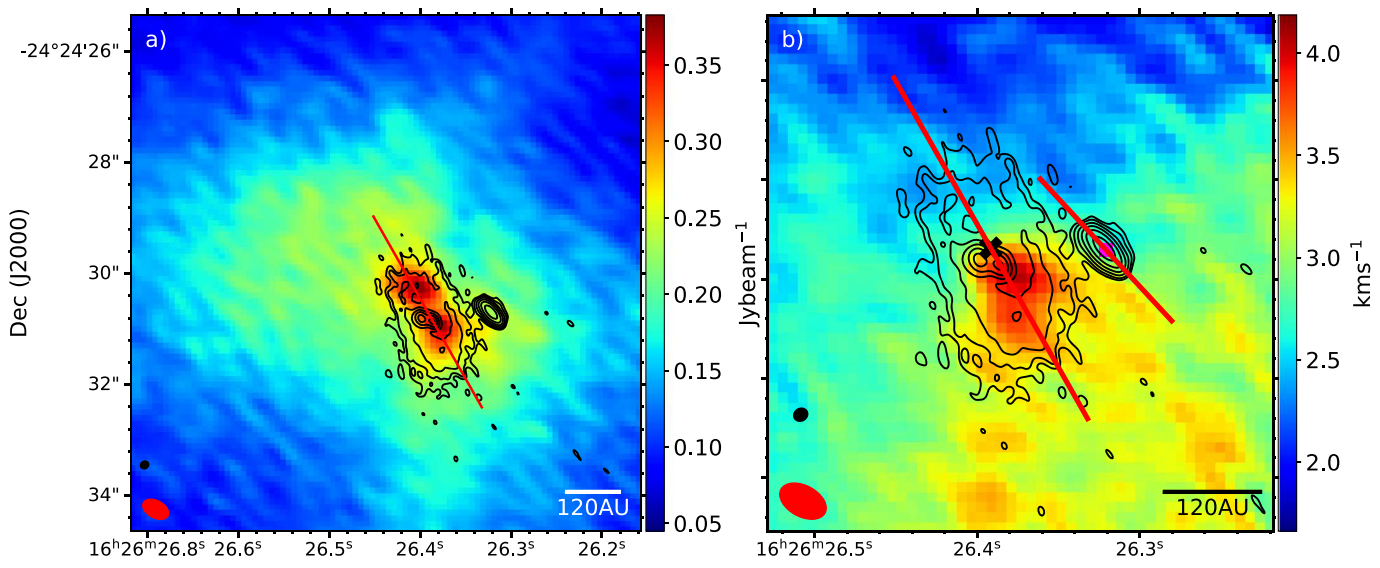


Figure 2. (a) VLA 1623 0.88 mm continuum (contours) overlaid on the Briggs -1.0 weighted $C^{18}O$ integrated intensity map (color). The color represents the $C^{18}O$ J=2-1 integrated intensity map (moment 0) using combined data from the ALMA 12 and 7 m arrays. The black contours are 0.88 mm continuum data in steps of 3σ , 5σ , 10σ , 20σ , 40σ , and 80σ , where $\sigma=5\times10^{-4}$ Jy beam $^{-1}$. The red line indicates the location of the PV cuts used in this study (P.A. = 209° 82, centered at VLA 1623A (α (J2000) = $16^h26^m26^\circ$ 390, δ (J2000) = $-24^\circ24'30''$ 688); P.A. = 222° 80, centered at VLA 1623B (α (J2000) = $16^h26^m26^\circ$ 305, δ (J2000) = $-24^\circ24'30''$ 705)). (b) VLA 1623 0.88 mm continuum (contours) overlaid on the Briggs -1.0 weighted $C^{18}O$ intensity-weighted velocity map (color). The positions of VLA 1623A and B are marked with a cross and a square, respectively.

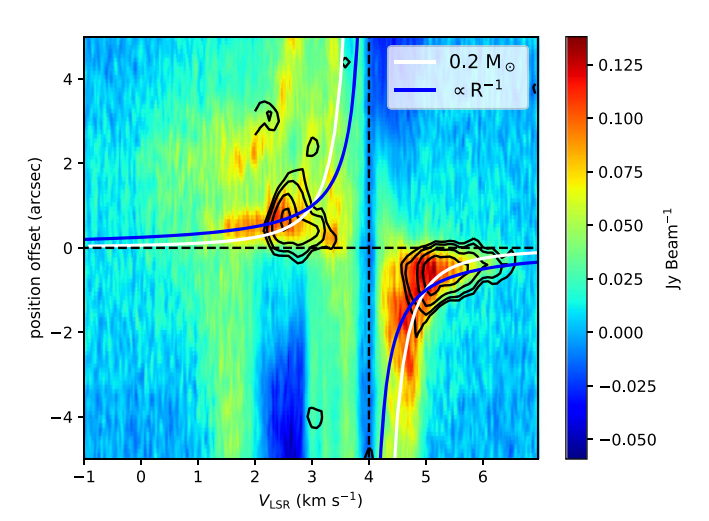


Figure 3. The VLA 1623A $C^{18}O$ J=2-1 PV diagram for Briggs -1.0. The black contours mark the ALMA Cycle 0 $C^{18}O$ J=2-1 data, and the color background represents ALMA Cycle 2 $C^{18}O$ J=2-1 data. The blue line represents the infall velocity profile with conserved specific angular momentum. The white line represents the Keplerian rotation profile with a central mass of $0.2 \, M_{\odot}$.

The C¹⁸O mean velocity map (Figure 2(b)) shows a rotating disk around VLA 1623A. In this study, all of the position-velocity (PV) diagrams will be aligned along the red line in Figure 2. The combined natural weighted C¹⁸O data for the 12 m array configurations C34-5 (baseline range 18.9–1090 m) and C34-1 (baseline range 14.2–347.3 m) and 7 m array (baseline range 7.1–48.9 m) data will be used in the analysis.

As for the Total Power Array data, the angular resolution is 29.67×29.67 (P.A. = 0.0) with an rms noise level of 0.5 Jy beam⁻¹. The script provided by the ALMA Regional Center is used to calibrate and reduce the data. The Total Power Array data would be used to identify the large-scale emission in the foreground, as well as the background of the VLA 1623A circumbinary disk.

2.3. Continuum Data

We use the high-resolution continuum data from the ALMA Archive (project ID: 2015.1.00084.S; PI: Leslie Looney); see Table 1. The observation is done in Band 7 with an integration time of 4798 s. The continuum data are prepared by using the CASA task CLEAN with uniform weighting. The synthesized beam is 0.13×0.12 (P.A. = 31.00) with an rms noise level of 0.5 mJy beam⁻¹.

2.4.
$$DCO^{+}J = 3-2 Data$$

The DCO+ data used in this paper are from ALMA Cycle 2 observations in Band 6 of the 12 m array combined with the observation from the 7 m array (project ID: 2013.1.01004.S; PI: Shih-Ping Lai). The data are prepared by the CASA task CLEAN with a weighting parameter of robust -0.5, and the UV taper range is set to 1."0. The rms noise level of the DCO+ data is 5 mJy beam $^{-1}$, and the synthesis beam size is 0."51 \times 0."31 (P.A. = 63.05). The velocity resolution of the DCO+data is 0.085 km s $^{-1}$.

2.5. SO (
$$\nu = 0$$
, $J = 8_8 - 7_7$) Data

In this paper, we present the results of the newly released ALMA Cycle 4 SO $\nu=0$, $J=8_8-7_7$ archival data (project ID: 2016.1.01468.S; PI: Victor Magalhaes) to trace accretion shocks (see Table 1). The observation was carried out by ALMA on 2017 March 4 with a maximum UV baseline of ~250 m. The data are calibrated by the ALMA calibration script, and the imaging is carried out via the CASA task CLEAN with a weighting parameter of robust 0.0. The resulting synthesized beam has an angular resolution of 1.11 × 0.176 (P.A. = 82.59) with an rms noise level of 20 mJy beam 1. The largest recoverable angular scale is around 3.15. The spectral resolution is 0.212 km s 1, and the SO ($\nu=0$, $J=8_8-7_7$) data have a line width larger than 8 km s 1, resulting in a line-to-channel width ratio of ~37.

 Table 1

 Summary of the Observational Data Used in the Analysis

Line	Transition	ν (GHz)	Beam Size (arcsec)	Maximum Recoverable Scale (arcsec)	Channel Widths (km s ⁻¹)	rms noise (mJy beam ⁻¹)	PI
CO	3–2	345.79599	0."99 × 0."59	4."33	0.0529	11	Cheng-Han Hsieh
$C^{18}O$	2-1	219.56036	0.752×0.731	23."26	0.0832	9	
			$1.''10 \times 0.''89$	23."26	0.0208	18	Shih-Ping Lai
			0.51×0.31	23."26	0.0208	14	
DCO+	3–2	216.11402	0.751×0.731	23."26	0.085	5	Shih-Ping Lai
SO	$\nu = 0$,	344.31061	$1.''11 \times 0.''76$	3."9	0.212	20	Victor
	$J = 8_8 - 7_7$						Magalhães
Continuum		336.50000	$0.''13 \times 0.''12$	0."88	53,309.11	0.5	Leslie Looney
Total Power Array	•••	219.56036	$29\rlap.{''}67 \times 29\rlap.{''}67$	427."86	0.0208	500	Shih-Ping Lai

3. Analysis

3.1. The Comparison between Cycle 0 and Cycle 2 Data

Figure 3 shows the comparison between the Cycle 0 (project ID: 2011.0.00902.S; PI: Nadia Murillo) and Cycle 2 (project ID: 2013.1.01004.S; PI: Shih-Ping Lai) ALMA data. In the Cycle 2 data, shown as the color background, we identified high-velocity blueshifted emission around 1.5 km s⁻¹, and the redshifted emission extends to 4."0. These features do not appear in the Cycle 0 observations because there is not enough sampling in the short baselines.

Cycle 0 consists of only 16 antennas with a maximum baseline of ${\sim}400$ m. The beam size is around $0\rlap.{''}79\times0\rlap.{''}61$ with a velocity resolution of 0.0833 km s $^{-1}$ (Murillo et al. 2013). The largest recoverable angular scale is around $2\rlap.{''}46$. In comparison, Cycle 2 observations have increased sensitivity from the larger number of antennas and larger recoverable scale. More $C^{18}O$ emission is recovered. Thus, the previous disk size and the structure of the VLA 1623A Keplerian disk need to be reanalyzed.

3.2. PV Diagram

To study the gas kinematics, we create PV diagrams centered at VLA 1623A along the red line shown in Figure 2 (α (J2000) = $16^{\rm h}26^{\rm m}26^{\rm s}390$, δ (J2000) = $-24^{\circ}24'30''.688$, P.A. = $209^{\circ}.82$) with a central velocity of $4.0~{\rm km~s^{-1}}$. Since the binary separation is within our beam size, the results are the same when we shift the PV cut from one component to the other. Thus, we select the center of C¹⁸O emission for our PV diagrams. From the rotation curves, the Keplerian rotation with a central star mass of $0.2~M_{\odot}$ and an inclination angle of 55° generally fits the PV data quite well. This is consistent with the results of Murillo using Cycle 0 data. Thus, we first set the combined mass for the VLA 1623A1 and VLA 1623A2 binary to be $0.2~M_{\odot}$ for flat and flared disk modeling.

In the high-velocity blueshifted part, we observed a strong emission above the Keplerian rotation white line (marked by a red arrow in Figure 4). The emission between 1.5 and 2.0 km s⁻¹ is reasonably well fitted with the infall line (with conserved angular momentum). This feature has not been seen in the Cycle 0 observation. The scaling of the conserved angular momentum line was set such that the crossover point with the Keplerian curve is located at the centrifugal radius of the disk. The corresponding specific angular momentum is 120 au km s⁻¹. The detailed estimation of the centrifugal radius is shown in Appendix A.

Is this high-velocity blueshifted component part of the Keplerian disk? Is it due to a flared Keplerian disk with projection effects? Or is it due to accretion flows or other large structures in the line of sight? To determine the nature of this super-Keplerian rotation component, we will conduct an analysis to identify large-scale cloud emission, accretion flows, large-scale structures, and the flared Keplerian disk.

3.3. Large-scale Emission around VLA 1623

The total power spectrum data are used to determine the strength and velocities of the gas corresponding to the largescale emission around VLA 1623. We did not combine the Total Power Array data with the 12 m + 7 m array data in order to separate the compact disk emission from the large-scale cloud emission. In Figure 5, five Gaussian functions are used to fit the total power spectrum with the best-fit result shown in Table 2. The main component identified from the Total Power Array (3.632 km s⁻¹) is closed to the system velocity and has an intensity that is significantly larger than the other extended emission. We therefore associate the maximum component at velocity 3.632 km s⁻¹ with the cloud emission of the VLA 1623 system. In Figure 3, at the system velocity 4.0 km s^{-1} , the C¹⁸O suffers huge absorption; this is consistent with our Gaussian fitted extended emission component 2, shown in Figure 5. The coincidence of vertical gaps in the PV diagrams and the Total Power Array components suggest that these vertical gaps resulted from the spatial filtering of extended emission. In all of the C¹⁸O PV diagrams, we combined both the 12 and 7 m arrays to have a maximum recoverable scale up to ~ 23.73 (~ 2760 au). The disk emission and accretion flows are well covered in this range. The Total Power Array traces extended emission at scales from ~ 29.77 (~ 3350 au) to \sim 427."9 (\sim 51,350 au). Any emission only observed in the Total Power Array is unlikely to have originated from the compact disk or accretion flows.

For other minor components located at velocities of 3.104, 2.029, and 2.561 km s⁻¹, their physical origins and whether or not they are part of the VLA 1623 system are unclear. Furthermore, all of the filtered large-scale emission in the PV diagrams, including the central envelope, is located in the blueshifted region, which is consistent with the preliminary estimations done by Murillo et al. (2013).

The Total Power Array data (large-scale emission) are not included in the flat and flared disk models (Sections 3.5 and 3.6). Since large-scale emission corresponds to scales much larger than the disk or accretion flows, it is unlikely to originate

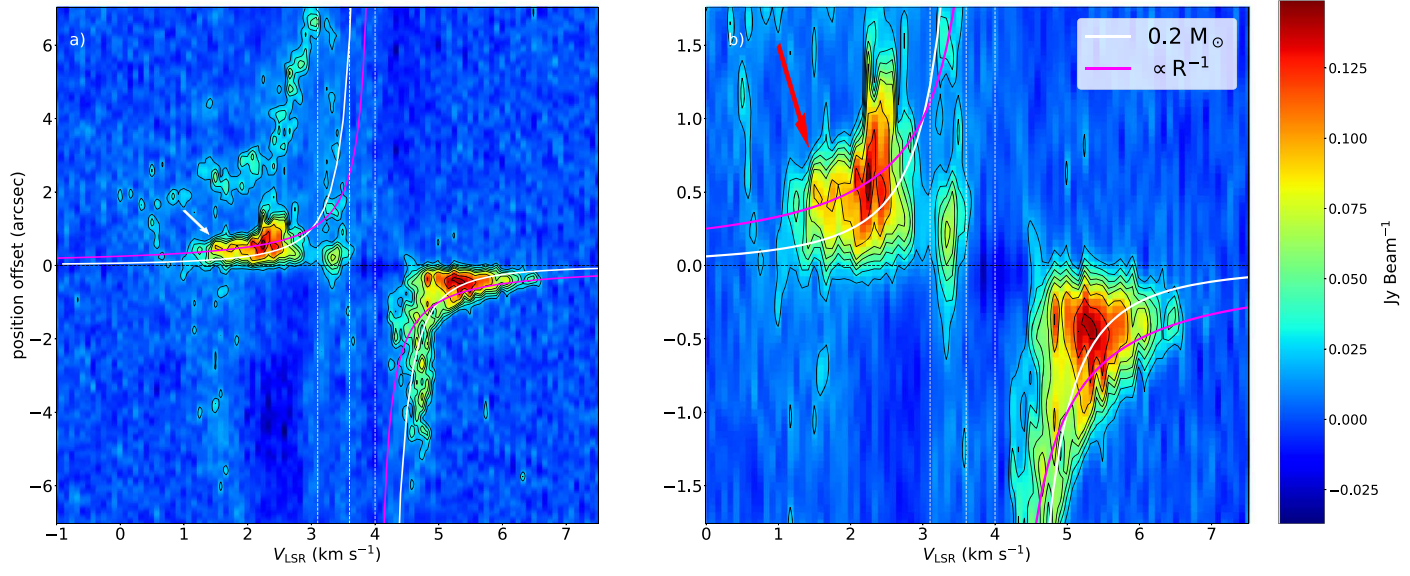


Figure 4. (a) PV cut of the natural weighted $C^{18}OJ = 2-1$ ALMA Cycle 2 VLA 1623A Keplerian disk, centered at VLA 1623A with a position angle of 209°82. The magenta line represents the infall velocity profile with a conserved specific angular momentum. The white line represents the Keplerian rotation profile with a central mass of $0.2 M_{\odot}$. The white arrow marks the position of a gap between accretion flow and the Keplerian disk. The vertical white dotted lines mark the velocity of the major filtered-out large-scale emission. (b) Zoomed-in image of panel (a). Note that the red arrow highlights a super-Keplerian rotation region.

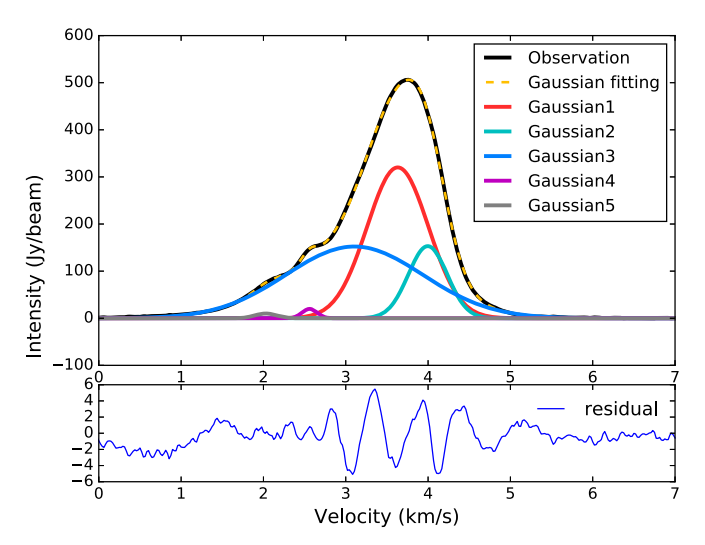


Figure 5. Gaussian fit of a total power spectrum of VLA 1623. The black line represents the observational data for the Total Power Array, and the colored lines represent the Gaussian fitting result.

Table 2
Total Power Spectrum Fitting Results (Large-scale Emission)

Number	Velocity $(km s^{-1})$	Amplitude (Jy)	Widths (km s ⁻¹)
1	3.632	320.19	0.2782
2	3.996	153.11	0.1117
3	3.104	152.29	1.3790
4	2.561	19.87	0.0164
5	2.029	10.04	0.0348
	$\sigma = 0.353 \text{ (Jy)}$	$\chi^2 = 9401.49$	$\chi^2/\text{dof} = 29.29$

from the disk emission, and the low spatial resolution of the data would bias the modeling. The purpose of this Total Power Array data fitting is to identify the velocity of large-scale emission. When comparing the data with models, we will avoid these components.

3.4. Using Dendrograms to Identify Accretion Flows and Set Constraints on Disk Size

A class 0 protostar is actively accreting and still deeply embedded in the envelope (Seifried et al. 2015). With infalling streamers feeding material from the envelope onto the circumbinary disk and outflows, it is challenging to identify disks around class 0 sources. In order to determine the disk size in a class 0 source, we need to identify outflows, envelopes, accretion flows, and other large-scale structures. Outflows have been observed in ¹²CO by Andre et al. (1990), Dent et al. (1995), and Yu & Chernin (1997). The envelope, which is located at 3.6 km s⁻¹ fitted by the total power spectrum, can be separated out from the rest of the components in the velocity domain.

The C¹⁸O traces both the rotational disk and the accretion flows around it. The dendrogram algorithm is used to identify the connected structures in the position–position–velocity (PPV) space (P.-I. Cheong et al. 2020, in preparation; see Figure 6). The algorithm identifies a total of eight major branches (local maximum), labeled in Figure 6. In addition to the six major branches found in P.-I. Cheong et al. (2020, in preparation), we found two more large structures, the blue-shifted III and VIII components, connected to the VLA 1623A circumbinary disk. In the following sections, we use SO as a shock tracer to identify the interactions between accretion flows and the circumbinary disk (see Table 3).

Besides the blueshifted III and VIII components, P.-I. Cheong et al. (2020, in preparation) further compared the data with the CMU model (Ulrich 1976; Cassen & Moosman 1981), a rotating collapse model with conserved specific angular momentum, and found that the redshifted VI and blueshifted I components are accretion flows connected to the central Keplerian disk (channel maps shown in Figures 7 and 8).

Figure 7 shows the channel maps of the blueshifted I component identified by the dendrogram. The 0.88 mm continuum data are shown as the magenta contours, which mark the location of the VLA 1623A circumbinary disk and VLA 1623B. Inside the magenta contours, the C¹⁸O emission

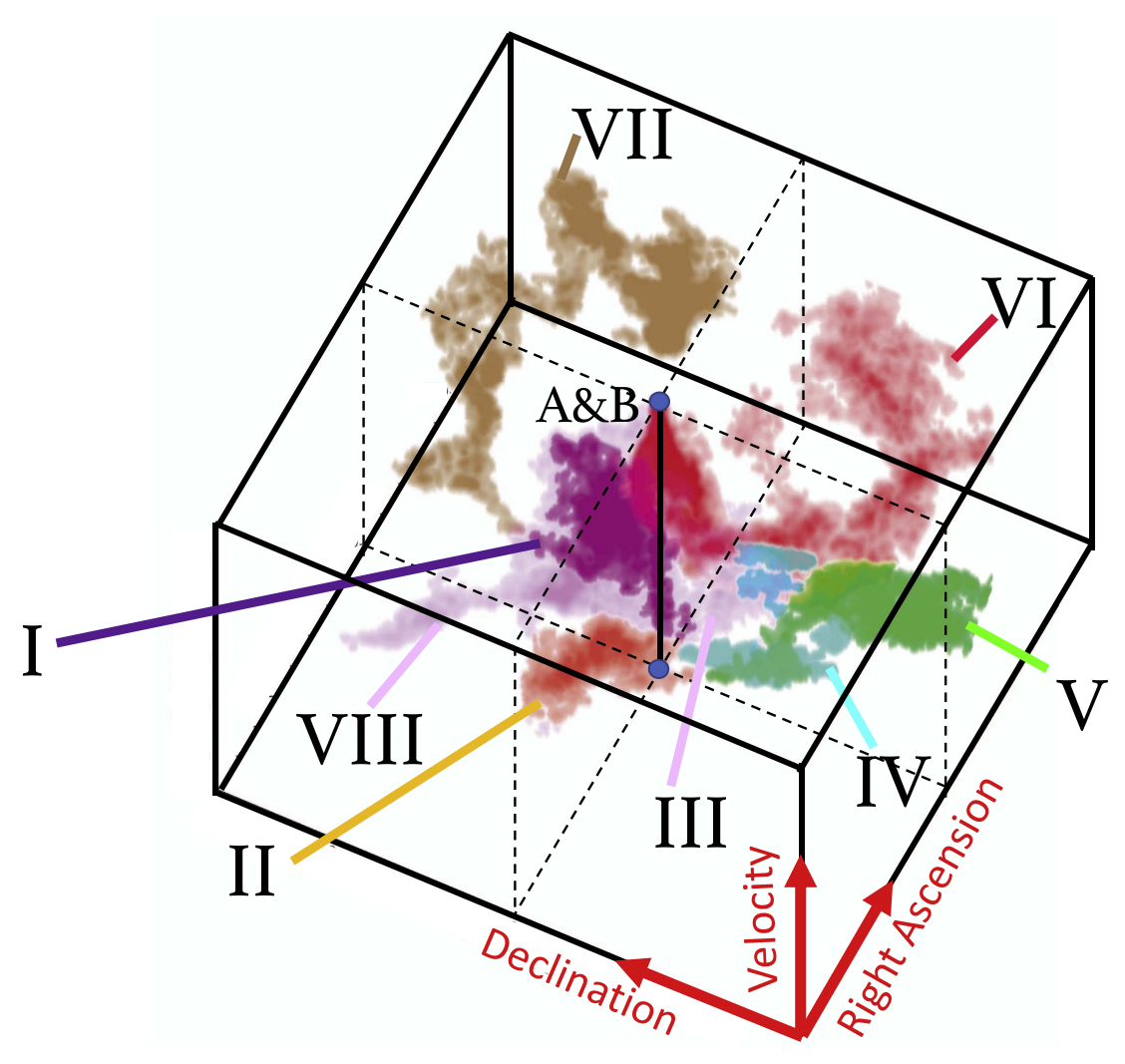


Figure 6. The 3D dendrogram around the VLA 1623 system. The C¹⁸O large structures are labeled with Roman numerals. The central black solid line marks the position of VLA 1623A and VLA 1623B in the PPV cube; VLA 1623A and VLA 1623B are very close to each other, with a separation within the blue dot. The 3D image is made by using GLUE visualization software (Beaumont et al. 2014). For a detailed analysis of the dendrograms, see P.-I. Cheong et al. (2020, in preparation).

Table 3
Accretion Flows around VLA 1623A

Structure	Velocity (km s ⁻¹)	SO Data	C ¹⁸ O Data
Accretion flows I	2.02-3.60	Figure 11 eastern SO stream	Figure 7
Outflow cavity wall II	1.27–2.21	Figure 11 southern SO stream	Figure 12(b) southern C ¹⁸ O stream
Accretion flows III	1.27–2.21	Figure 11 northern SO stream	Figure 12(b) northern C ¹⁸ O stream
Accretion flows VI	3.45–4.79	Figure 11 western SO stream	Figures 8, 12(a) western C ¹⁸ O clump
Outflow cavity wall 2.95–3.29 VIII		Figure 14 channel 3.084 km s ⁻¹	Figure 16

shows that the blueshifted I accretion flows are faintly connected to the central disk. The drop of C¹⁸O intensity between the disk and large structure I indicates that a clear gap around 120 au exists between the large-scale structure and the Keplerian disk. The Keplerian disk is constrained to roughly 180 au from the blueshifted channel maps.

Figure 8 shows the channel maps of the redshifted accretion flow VI connected to the central disk. In the velocity channels between 4.17 and 5.00 km s $^{-1}$, the accretion flow is well mixed with the disk, and the $C^{18}O$ emission extends to 6.0 ($\sim\!500$ au). Only in the high-velocity channels (>5.1 km s $^{-1}$) does the $C^{18}O$ emission trace the Keplerian disk without any contamination from the accretion flow. High-velocity channels are not contaminated by accretion flows, but they only provide the information in the inner region of the Keplerian disk. Thus, the disk size cannot be determined by the redshifted channels.

From the rotation curves in Figure 4, we deduce that the motion of the disk is Keplerian. Hence, without loss of generality, we can assume that the disk is axially symmetric and use the blueshifted side to constrain the disk size. We select

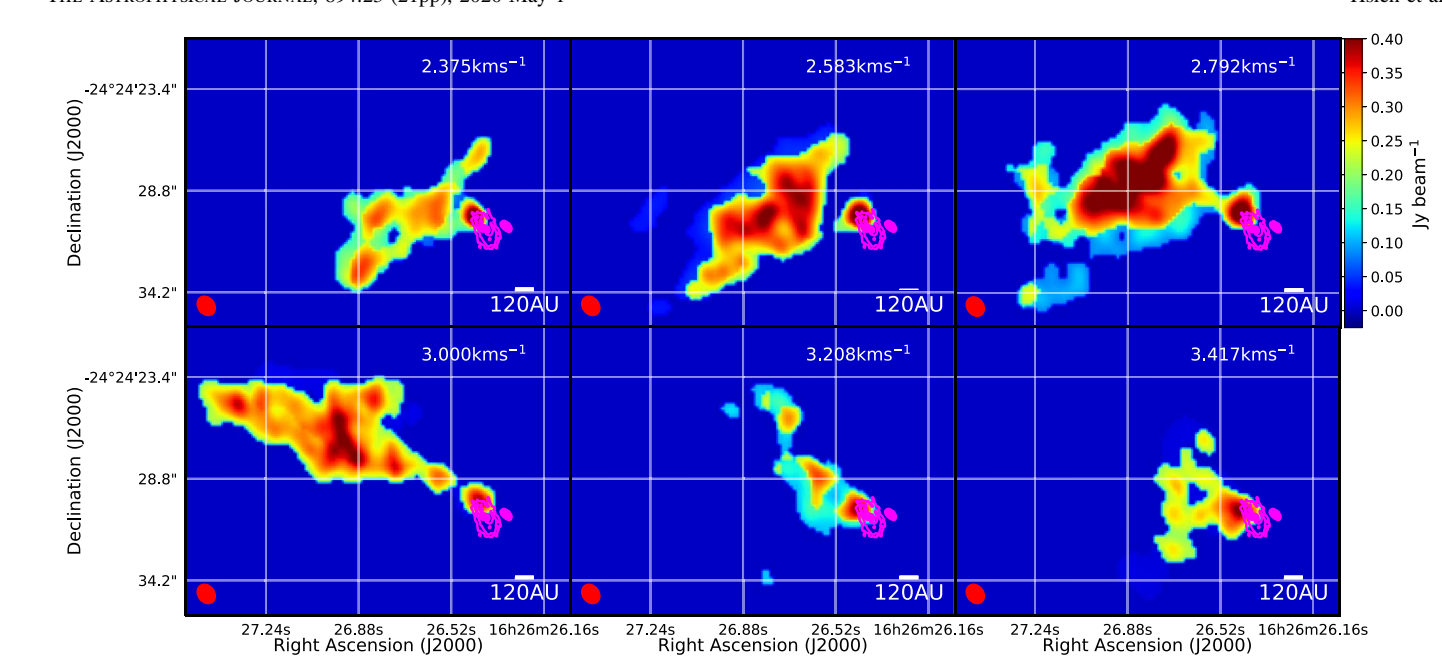


Figure 7. The VLA 1623A and blueshifted accretion flow I channel maps. The colors represent the $C^{18}O$ J=2-1 emission (Briggs -1.5) identified by the dendrogram algorithm. The dendrogram corresponds to the purple component (accretion flows and disk) in P.-I. Cheong et al (2020, in preparation). The magenta contours are 0.88 mm continuum data. The contours are in steps of 3σ , 5σ , 10σ , 20σ , 40σ , and 80σ , where $\sigma = 5 \times 10^{-4}$ Jy beam⁻¹).

the continuum level such that the edge of the disk matches the boundary of the gap in Figure 7. Therefore, the circumbinary disk size is constrained to be 180 au. Furthermore, the extended emission between 4 and 5 km s⁻¹ in Figure 3 is likely a mixture of accretion flow and disk components. We will explore this more in the following sections. More technical details of the dendrogram data preparation and accretion flow modeling can be found in P.-I. Cheong et al. (2020, in preparation).

3.5. Flat Disk Model

We first model the ALMA Cycle 2 $C^{18}O$ J=2-1 PV diagram of the VLA 1623A circumbinary disk with a flat Keplerian disk model. The PV diagram is cut along the red line in Figure 2. The governing equations for the velocity, temperature, and column density profiles in the flat Keplerian disk are described as follows:

$$v(R) = \sqrt{\frac{GM_*}{R}},\tag{1}$$

$$T(R) = T_0 \times \left(\frac{R}{100 \text{ au}}\right)^{-0.5},$$
 (2)

$$\Sigma(R) = \Sigma_0 \times \left(\frac{R}{100 \text{ au}}\right)^{-1}.$$
 (3)

For the column density at 100 au (Σ_0) , we adopted the number 6.173×10^{21} cm⁻², and the disk inclination angle is 55° (Murillo et al. 2013). For temperature distribution, we assumed the temperature power-law exponent to be -0.5, and we adopted a temperature of ~ 30 K at 100 au based on the DCO⁺ 5-4/3-2 data (Murillo et al. 2018).

A flat disk model is first generated using Equations (1)–(3). A simple ray-tracing radiative transfer calculation scheme assuming local thermal equilibrium with a thermal broadening of 0.2 km s⁻¹ is used to generate the synthetic images in PPV

space. Then, the simulated disk is convolved with the ALMA telescope beam using CASA SimObserve and SimAnalyze. The exact antenna setup for C34-1, C34-5, and two ACA observations is input into SimObserve to recreate the exact beam used in the observation.

From the PV diagram shown in Figure 9(a), we found that the peak location of the flat disk model has a significant offset compared to the data. The flat disk model has a peak located at a 0.18 position offset, while the observational data have a peak located at a 0.15 position offset on the redshifted side. No emission was detected in the observational data corresponding to the flat disk model's blueshifted peak, and this is consistent with the filtering of the large-scale emission at 3.1 km s⁻¹ fitted by the total power spectrum.

We plot both the infall with conserved angular momentum and Keplerian rotation curves in Figure 9(a). In the outer region of the disk, the white Keplerian line passes through the flat Keplerian disk model and the observation data on the redshifted side for a position offset within 2."5. However, in the corresponding zoomed-out PV diagram in Figure 4(a), for a position offset greater than 2."5, the white Keplerian rotation line clearly deviates from the data. Thus, it is very likely that the C¹⁸O long tail between 2."5 and 5."0 corresponds to materials at system velocity slowly infalling toward the circumbinary disk.

3.6. Flared Disk Model and the Constraint of the VLA 1623 Circumbinary Disk's Vertical Scale Height

A more sophisticated 3D flared disk model is further developed to constrain the density profile and the physical structure of the circumbinary disk around VLA 1623A. We followed the equations of Guilloteau & Dutrey to develop a 3D flared disk model (Guilloteau & Dutrey 1998; Yen et al. 2014). The density, velocity, and temperature profile are given as

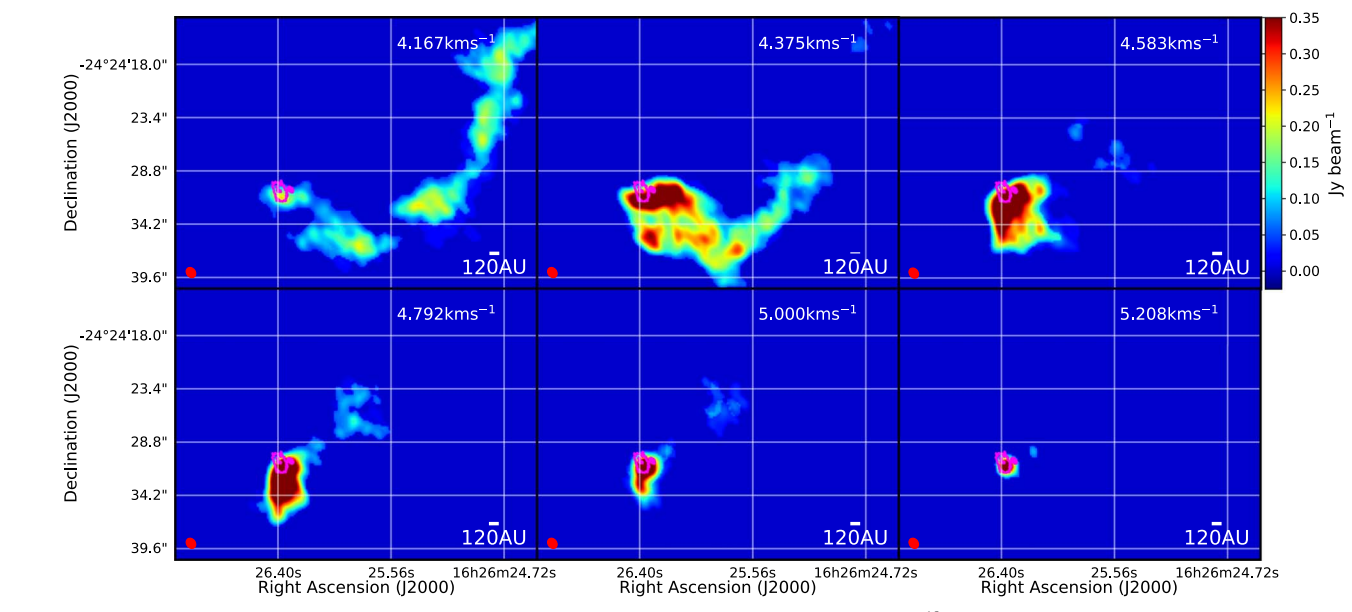


Figure 8. The VLA 1623A and redshifted accretion flow VI channel maps. The colors represent the $C^{18}O$ J=2-1 (Briggs -1.5) emission identified by the dendrogram algorithm. The dendrogram corresponds to the red component (accretion flows and disk) in P.-I. Cheong et al. (2020, in preparation). The magenta contours are 0.88 mm continuum data. The contours are in steps of 5σ and 40σ , where $\sigma = 5 \times 10^{-4}$ Jy beam⁻¹.

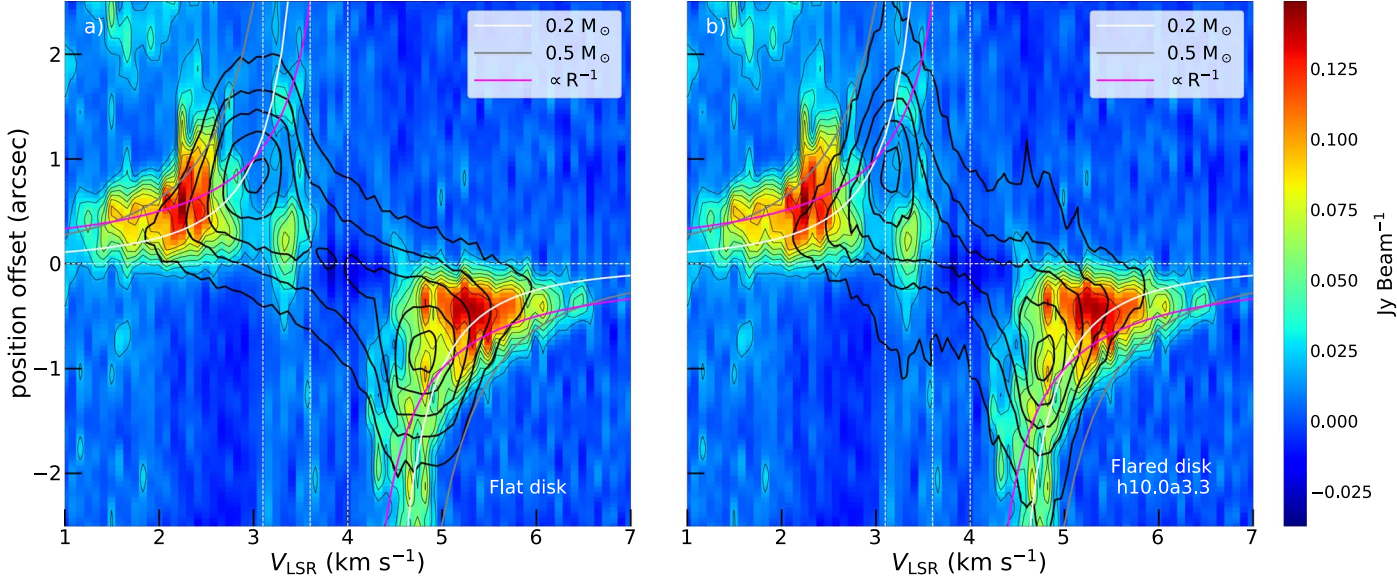


Figure 9. (a) PV diagram of the VL1623A Keplerian disk overlaid with flat disk model contours. The colors represent the PV diagram of the natural weighted $C^{18}O$ J=2-1 emission centered at VLA 1623A. The thick black contours outline the flat Keplerian disk model in steps of 5σ , 10σ , 20σ , 30σ , 40σ , 45σ , and 50σ , where $\sigma=6$ mJy beam⁻¹. (b) PV diagram of the VLA 1623A Keplerian disk overlaid with the best-fit flared disk model contours (vertical scale height $h_0=10.0$ and power-law index a=3.3). The thick black contours outline the flared Keplerian disk model in steps of 0.2, 0.4, 0.6, 0.8, and 0.95 of the maximum flux in the model. In both panels, the white and gray lines represent the Keplerian rotation curve with central star masses of 0.2 and $0.5 M_{\odot}$ and an inclination angle of 55° . The magenta lines represent the infall velocity profile with conserved specific angular momentum. The vertical white dotted lines mark the velocities of the major filtered-out large-scale emission. The color background represents the PV diagram of the natural weighted $C^{18}O$ J=2-1 emission centered at VLA 1623A, and the thin black contours plot 3σ , 5σ , 7σ , 9σ , 11σ , 13σ , and 15σ , where $\sigma=9$ mJy beam⁻¹.

follows:

$$\nu(R) = \left(\frac{GM_*}{R}\right)^{-\nu},\tag{4}$$

$$T(R) = T_0 \times \left(\frac{R}{100 \text{ au}}\right)^{-q},\tag{5}$$

$$\rho(R) = \rho_0 \times \left(\frac{R}{100 \text{ au}}\right)^{-a} \times \exp\left(-\frac{z^2}{2h(R)^2}\right). \tag{6}$$

The scale-height relationship is given as

$$h(R) = h_0 \times \left(\frac{R}{100 \text{ au}}\right)^b, \tag{7}$$

where h_0 is the scale height of the circumbinary disk at 100 au, and b is the flaring index. Assuming hydrostatic equilibrium, the scale height b = 1 + v - q/2 with v = 0.5 and q = 0.4 for a theoretical flared Keplerian disk (Guilloteau et al. 2011). The value of b is set to 1.29 using the theoretical model of the

flared disk (Chiang & Goldreich 1997). The value of a follows a = p + 1 + v - q/2 = 1.3 + p, with p being the power-law index of the surface density $\Sigma = \Sigma_0 r^{-p}$ (Guilloteau & Dutrey 1998). Considering the typical range for the surface density power law $1 \le p \le 2$, we explore the density power-law index a in the range between 2.0 and 4.0.

In our simple flared disk model, we set the C^{18} O-to- H_2 ratio to be 1.7×10^{-7} . The resolution of the model is $500 \times 500 \times 500$ with each pixel at a resolution of 0.72 au. For the density profile, we normalized the ρ_0 such that the total mass of the circumbinary disk is $0.02~M_{\odot}$ (P.-I. Cheong et al. 2020, in preparation). The disk size is set to be 180 au in radius, as constrained from the C^{18} O data. The inclination angle is 55°, and the distance is at 120 pc (Loinard et al. 2008; Murillo et al. 2013).

We apply the RADMC-3D radiative transfer code to the flared disk model to create synthetic images in 3D Cartesian geometries with a channel width set to 0.060 km s⁻¹ (Dullemond et al. 2012).¹⁰ The synthetic images are then convolved with the ALMA telescope beam using CASA SimObserve and SimAnalyze. Since we are interested in the density structure (a) and vertical structure (h_0) of the flared circumbinary disk, we fixed the temperature T_0 to be 30 K at 100 au based on the DCO⁺ data (Murillo et al. 2018).

Figure 10 displays various flared disk models with different density power-law indexes a and the vertical scale-height parameters h_0 for the redshifted side of the disk. Comparing the models in Figures 10 and 20 with observation data is very challenging. The total power spectrum reveals huge large-scale emission at velocity 4.0 km s⁻¹ (systematic velocity) and much more on the blueshifted side. Therefore, in order to eliminate the contamination of the large-scale cloud and foreground and background emission, we only model the redshifted part on the right side of the line corresponding to system velocity 4.0 km s⁻¹. Furthermore, to avoid contamination from the outer accretion flows, we only compare the data and model within the disk radius ($\leq 1...^{\prime\prime}5$).

Isophote contours for each simulation model are plotted in order to compare the observational data with simulation models. Overall, we run the parameters $h_0 = 1.0$, 2.5, 5.0, 10.0, 15.0, and 25.0 (au) and a = 2.0, 2.3, 2.6, 3.0, 3.3, and 4.0 for a total of 36 parameter combinations to examine how the central peak location changes when the scale height h_0 and the density power-law index a are varied.

In Figure 10, as the vertical scale height h_0 increases, the model's peak (thick black contours) shifts toward the connecting bridge between the blueshifted and redshifted regions (system velocity 4 km s⁻¹ and offsets 0.0). As for the density power-law index a, when a increases, the PV diagram will be stretched in the direction of the Keplerian rotation line (white line). This is because when a increases, the extended part of the disk will be suppressed, and the intensity peak will move closer to the disk center.

At first sight, the best-fit model would be the one with a density power-law index a = 4.0 and scale height $h_0 = 25.0$. The density power-law index a = 4.0 suggests that the peak is very compact in the center of the circumbinary disk VLA 1623A. In the very high velocity regions v > 6.0 and <2.0 km s⁻¹, the observation data deviate from the flared disk model

and do not follow the white Keplerian rotation line. This deviation suggests that an inner compact structure exists inside the VLA 1623A circumbinary disk. To avoid the contamination from the inner super-Keplerian region when constraining the circumbinary disk properties, we only model the data outside the inner region (\sim 0." 5 (60 au)) where the inner structure of VLA 1623A lies.

For the model with parameters a = 4.0 and $h_0 = 25.0$, we found that the peak of the flared disk model has the same position offset (\sim 0."5) as the observation data but at a much lower velocity (4.9 km s⁻¹ as compared to 5.2 km s⁻¹). The peak of the flared disk model and the observational data do not overlap, suggesting that the circumbinary disk does not have a density power-law index a as large as 4.0. Instead, it has a relatively flatter density power law plus a compact inner structure within 60 au from the disk center.

For a density power-law index a less than 3.3, there are only minor differences when a varies. The PV diagram overall is insensitive to parameter a. To prevent contamination of large-scale emission and internal structures, we search for disk models with parameter $a \le 3.3$, peak locations between 0."5 and 1."5 in position offset, and emission between 4.5 and 4.9 km s⁻¹.

Close inspection of the fitting reveals that when the vertical scale height $h_0=25.0$ au, the models have peaks located at velocities of 4.5–4.7 km s⁻¹ on the redshifted side. Most importantly, in all of the $h_0=25.0$ models, more than half of the peak area falls outside the 7σ (63 mJy; brown line in Figure 10) line on the redshifted side. This significant offset shows that $h_0=25.0$ does not fit the data. For vertical scale height $h_0=15$ au, the peak overlap area is around 20% for model $h_0=15$, $h_0=15$,

It is important to highlight again that for all of the parameter sets, no model can perfectly fit the location of the peak in the PV diagram. Both flat and flared disk models do not produce peaks at the same location as the observational data. Changing vertical scale height cannot produce high-velocity peaks in the inner region of the Keplerian disk, and adjusting the density power law only stretches the contours along the Keplerian rotational line. From the flat and flared disk modeling, we have shown that simple Keplerian rotation disk models with a combined binary mass of $0.2\,M_\odot$ cannot fully explain the observational data.

3.7. Limitations and Degeneracy in Modeling

Modeling and constructing a coherent picture from the complex data set around the class 0 source VLA 1623 is difficult, as multiple physical processes (outflows, infalls, rotation, shocks) need to be taken into account, and a wide range of parameters can be adjusted. Careful and logical reasoning is required to connect the pieces and form the overall picture. In this section, we will discuss the limitations and the logical reasoning behind breaking the degeneracy in the modeling.

¹⁰ RADMC-3D website: http://www.ita.uni-heidelberg.de/~dullemond/software/radmc-3d/.

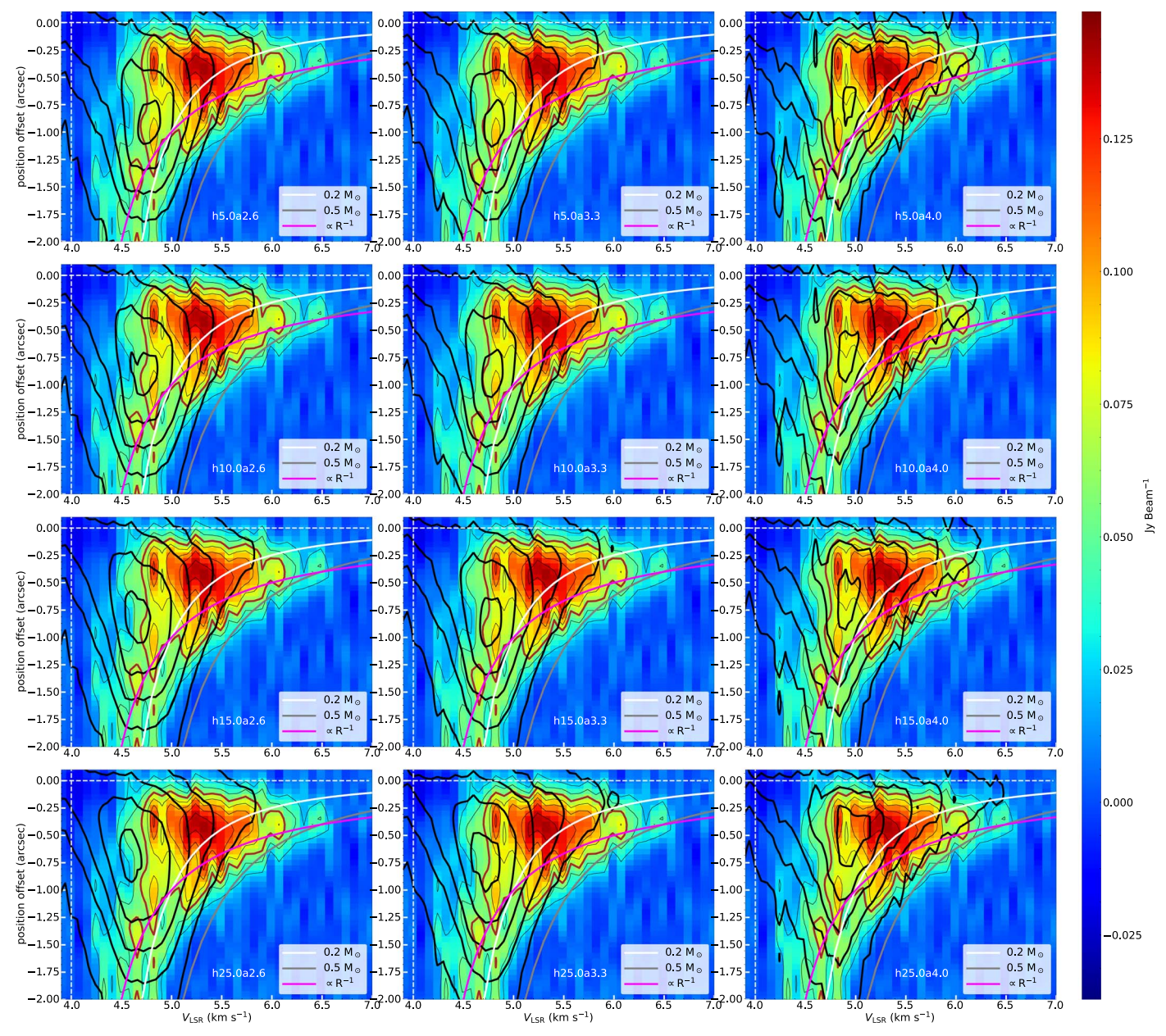


Figure 10. The PV diagram of the VLA 1623A Keplerian disk overlaid with the flared disk model contours (central binary mass: $0.2 M_{\odot}$) for different vertical scale heights h_0 and density power laws a. The colors represent the PV diagram of the natural weighted C¹⁸O J=2-1 emission centered at VLA 1623A, and thin black contours are plotted for 3σ , 5σ , 9σ , 11σ , 13σ , and 15σ with $\sigma=9$ mJy beam⁻¹. The brown contour marks the 7σ line used for model comparison. The thick black contours are from the flared Keplerian disk model. The contours are in steps of 0.2, 0.4, 0.6, 0.8, and 0.95 of the maximum flux in the model. The white and gray lines represent the Keplerian rotation curve with central star masses of 0.2 and 0.5 M_{\odot} and an inclination angle of 55°. The magenta line represents the infall velocity profile with conserved angular momentum.

3.7.1. Important Parameters and Limitations of the Disk Modeling

Since the flared disk model is used to constrain the disk properties (disk scale height and density power-law index), the discussion of important parameters and limitations of the disk modeling will be focused on the flared disk model.

In total, there are 10 parameters in the flared disk model: scale height, temperature profile (power-law index and normalization), density profile (power-law index and normalization), inner cutoff radius, disk inclination, disk size, combined binary mass, and distance. Two parameters, density profile (power-law index) and scale height, are free parameters that are explored and constrained. The other eight parameters and their effects on the PV diagram modeling (Figure 10) are listed below.

- 1. Temperature profile (power-law index). The profile affects the position of the peak in the disk by stretching the peak along the Keplerian rotation line in the PV diagram. This is the second-largest uncertainty in the modeling. It will be discussed more in Section 3.7.2. However, we do not expect a huge deviation from the theoretical flared disk model unless other heating or cooling mechanisms are present.
- Temperature normalization at 100 au. This affects the overall normalization of the flux. It does not change the peak position in the PV diagram and therefore has little or no effect on the scale height and density power-law modeling.

- 3. Density normalization (disk mass). This affects the overall normalization of the flux and has little or no effect on the peak position in the PV diagram. It is constrained by normalizing the disk mass to $0.02~M_{\odot}$ (P.-I. Cheong et al. 2020, in preparation).
- 4. Disk size. The gas disk size is \sim 180 au, constrained by the inner edge of the gap in Figures 4 and 7. Disk size affects the spatial size of the model in the PV diagram. This parameter is well constrained by observation and has an uncertainty around half of the beam size (\sim 30 au).
- 5. Inner cutoff radius. Since the disk is in Keplerian rotation, the closer to the protostar, the faster it rotates. The inner cutoff radius will determine the velocity cutoff point in the PV diagram. To prevent artificial velocity cutoff at high velocity, a small inner cutoff radius is chosen. In the inner region of the disk, since the area decreases with smaller radius, the intensity drops rapidly at the high-velocity end of the PV diagram. Therefore, for a small enough inner cutoff radius, the velocity cutoff would have little or no effect on the disk modeling. In flared disk modeling, the inner cutoff radius is set to be 1 au (cell size 0.72 au). As for the flat disk model, the inner cutoff radius is also 1 au.
- 6. Disk inclination. The inclination angle used in the modeling is 55° (Loinard et al. 2008; Murillo et al. 2013). The PV diagram is aligned along the major axis of the disk, so the change in inclination would have no effect on the direction of the position offset in the PV diagram. Inclination only affects the projection of velocity to the line of sight and stretches the model contours away from or toward the systematic velocity. Even for a 5° variation of the inclination angle, the velocity stretching factor is less than 7%. In Figure 10, for a density power-law index a < 3.3, the peak velocity difference between vertical scale height h = 15 and 25 au is $\sim 0.2 \,\mathrm{km \, s^{-1}}$. The peak velocities of the h = 25 au models are located around 0.6–0.7 km s⁻¹ away from the systematic velocity. If the h = 25 au models are stretched by 7%, the peak velocity will increase by $\sim 0.05 \text{ km s}^{-1}$ at most, which is still smaller than the $0.2 \,\mathrm{km \, s^{-1}}$ difference used to distinguish accepted and nonaccepted models. Thus, disk inclination in our modeling would not change the result of flared disk
- 7. Combined binary mass. This is the most important factor in the disk modeling. Not only will it significantly affect the results of flared disk modeling, it is also a possible explanation for the super-Keplerian rotation in the inner region of the disk. A more in-depth discussion about the degeneracy of the combined binary mass will be presented in Section 4.1.
- 8. Distance. In this paper, a distance of 120 pc (Murillo & Lai 2013) is used in the modeling instead of 137.3 pc (Ortiz-León et al. 2017). The physical scale will increase by a factor of 1.14 if the 137.3 pc distance is adopted. In Figure 10, for power-law index a < 3.3, the shapes of the model peaks are elongated in the direction of position offset. One major difference between vertical scale heights h = 15 and 25 au is that the centers of the peaks are located at different velocities. Stretching the models by 14% in position offset will make it harder to

differentiate between the two, but it will not change the result of the flared disk modeling.

3.7.2. Degeneracy in Temperature and Density Profile

The disk intensity profile is determined by both temperature and density. In this study, for the flared disk model, we assumed a fixed temperature profile with a power-law index of -0.4 based on the theoretical flared Keplerian disk model (Guilloteau et al. 2011). As for the normalization, we fixed the temperature to 30 K at 100 au based on the previous DCO⁺ modeling (Murillo et al. 2018).

Fixing the temperature profile greatly reduces the free parameters in the modeling. It is important to note that the temperature profile is based on a simple theoretical model, and in reality, the actual temperature profile might deviate from this fixed profile. If the power-law index is varied with the overall temperature normalization fixed at 100 au, one would expect the peak to move inward or outward depending on the power-law index. In other words, the peak will move along the Keplerian rotation line in the PV diagram. This will affect the density and scale-height modeling, making it even more difficult to break the degeneracy, but the model still will not be able to reproduce the observed peaks, which clearly deviates from the Keplerian rotation. Thus, it is not a good explanation for the super-Keplerian motion.

It will, however, affect the result of scale-height modeling. For a larger disk scale height, the peak will move closer to the position offset 0.0 (center of the disk) and toward the system velocity in the PV diagram. Adjusting the temperature power-law index would further stretch the peak along the Keplerian line. The two completing effects combined would make it very difficult to break the degeneracy. Even so, we do not expect the temperature profile to deviate too much from the theoretical flared disk model unless additional heating or cooling processes are involved.

The better and more accurate way to break the temperature and density degeneracy is to use two C¹⁸O transitions to obtain the temperature profile and constrain it directly from observation instead of using the simple theoretical model. Future observation is needed to more accurately constrain the temperature profile of the VLA 1623A circumbinary disk.

3.8. Accretion Shocks around the Circumbinary Disk

Generally, SO with a sublimation temperature of 50 K is attached to dust grains. Observation of SO emission indicates that it comes from collisions or shocks that give enough energy to free SO into the gas phase. Previously, SO emission was used to trace shock fronts in another similar class 0 disk system, L1527 (Sakai et al. 2014). In this section, we use SO as a shock tracer to understand the interactions between the accretion flows and the circumbinary disk.

Figure 11(a) shows the SO $\nu=0$, $J=8_8-7_7$ moment 0 map. A strong enhancement of SO molecules near the circumbinary disk and VLA 1623B is apparent in the moment 0 map, and this indicates that strong accretion shocks are created around the VLA 1623A circumbinary disk and VLA 1623B. The SO emission shows four stream-like structures with two main streams to the west and south. The southern stream has the strongest emission in all of the streams and is connected to VLA 1623B. The western stream corresponds to the redshifted accretion flow VI identified by the dendrogram

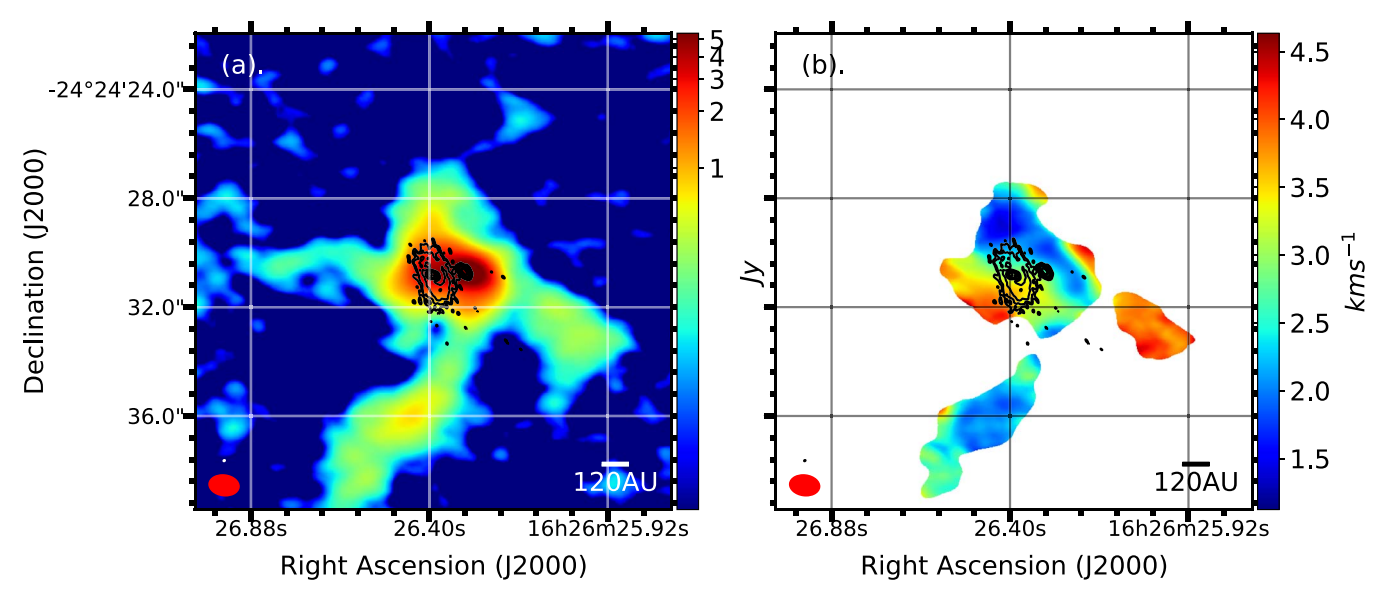


Figure 11. (a) SO intensity integrated map (moment 0). The colors represent the ALMA Cycle 4 SO $\nu=0$, $J=8_8-7_7$ data. The black contours are 0.88 mm continuum data. The contours are in steps of 3σ , 5σ , 10σ , 20σ , 40σ , and 80σ , where $\sigma=5\times10^{-4}$ Jy beam $^{-1}$. (b) SO mean velocity map (moment 1).

analysis using C¹⁸O, and the eastern stream corresponds to the blueshifted accretion flow I in Figure 6 (red and purple accretion flow, respectively, in P.-I. Cheong et al. 2020, in preparation).

Both the southern and western streams connect to VLA 1623B, and a strong emission of SO is detected on VLA 16232B. The SO peaks at VLA 1623B and the stream morphology suggest that on VLA 1623B, there exist violent shocks caused by the collision between B and the outer redshifted accretion flow VI. As for the northern and eastern streams, they connect to the VLA 1623A circumbinary disk on the map in the plane of the sky. The northern stream is much shorter than the southern stream, and this indicates that the collision is much closer toward VLA 1623A and VLA 1623B from the north. In the southern stream, the peak locates around 7.0 south of the VLA 1623A binaries.

Figure 11(b) shows the mean velocity map (moment 1) of SO emission around the VLA 1623A circumbinary disk and VLA 1623B. Notice that the system velocity of the VLA 1623A circumbinary disk is 4 km s⁻¹, and nearly all of the SO in the moment 1 map does not have a velocity greater than 4.4 km s⁻¹. The lack of redshifted emission in the northern SO stream shows that it corresponds to the blueshifted accretion flow III (Figure 6) toward the circumbinary disk. The extended high-velocity SO emission in the northern stream is caused by the accretion shocks due to the collision between the circumbinary disk and accretion flow.

As for the southern SO stream, it lies in the position corresponding to the redshifted accretion flow VI (Figure 8). However, the accretion flow VI traced by $C^{18}O$ is observed to be redshifted and moving away from the observer, while the SO southern stream is blueshifted and moving in the opposite direction. For comparison between $C^{18}O$ and SO data, we plot the $C^{18}O$ J=2-1 intensity integrated map (moment 0) between 3.29 and 4.43 km s⁻¹ in Figure 12(a) and between 1.27 and 2.21 km s⁻¹ in Figure 12(b), with the SO data displayed as black contours in both figures.

In Figure 12(a), the C¹⁸O emission that corresponds to the materials at low blueshifted velocity and at rest is much more extended than the southern SO stream. The C¹⁸O at rest is

mostly distributed on the south side of the circumbinary disk and VLA 1623B. Materials are piled up in the south, and this wall-like structure will be discussed in the next section.

Among the most prominent features in Figure 12(b) are the northern and southern arms. The northern C¹⁸O arm corresponds to accretion flow III (see Figure 6). The southern C¹⁸O arm has the same velocity range as the SO southern stream, and it overlays the line of sight perfectly. From the dendrogram analysis carried out by P.-I. Cheong et al. (2020, in preparation), the southern arm corresponds to structure II in Figure 6. P.-I. Cheong et al. (2020, in preparation) further carried out the CMU model analysis (Ulrich 1976; Cassen & Moosman 1981), a rotating collapse model with conserved specific angular momentum, and found that the blueshifted component II does not match the CMU model. This indicates that the materials in the southern stream do not follow the infalling parabolic trajectories. From the dendrogram analysis and CMU fitting in P.-I. Cheong et al. (2020, in preparation), we concluded that the southern SO stream of Figures 11(a) and (b) corresponds to the materials with nonconserved specific angular momentum, possibly affected by outflows from the protostellar sources.

To confirm this interpretation, we plot the CO outflows on top of the SO shock emission in Figure 13. The black contours represent the 0.88 mm continuum data. The center of the bipolar outflow coincides with VLA 1623B, hinting that VLA 1623B might be the origin of the outflow. The northern, eastern, and western SO streams are further away from the outflow direction, making them more likely to be tracing the accretion shocks from the accretion flows than the shock fronts of the outflows. As for the southern SO stream, it perfectly overlays the CO outflow, suggesting that the SO southern stream is tracing the collision between outflow and outflow cavity walls. The distribution of shocks in both position and velocity space is further shown as SO channel maps in Figure 14.

After identifying the corresponding SO streams around the VLA 1623A circumbinary disk by comparing with the C¹⁸O data, PV diagrams are used to further study their interactions. We plot the PV diagrams of SO $(J = 8_8-7_7)$, C¹⁸O (J = 2-1),

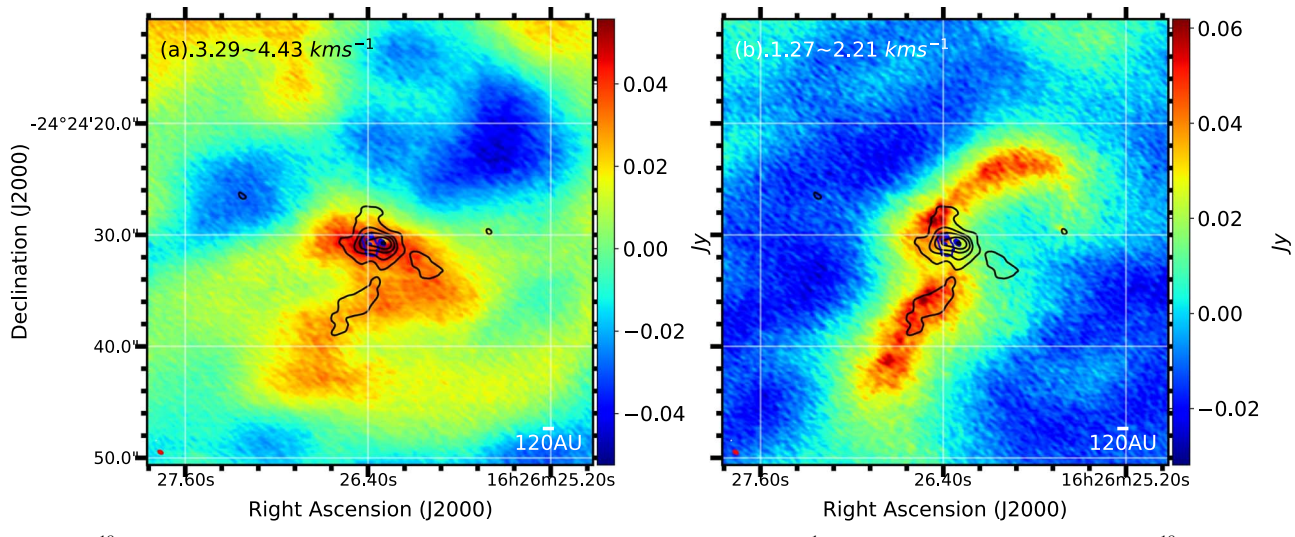


Figure 12. (a) $C^{18}O$ J=2-1 intensity integrated map (moment 0) between 3.29 and 4.43 km s⁻¹ for Briggs -1.0 weighted data. (b) $C^{18}O$ J=2-1 intensity integrated map (moment 0) between 1.27 and 2.21 km s⁻¹ for Briggs -1.0 weighted data. The colors in both panels represent the $C^{18}O$ data. The black contours are ALMA Cycle 4 SO $\nu=0$, $J=8_8-7_7$ data. The contours are in steps of 0.025, 0.05, 0.1, 0.2, 0.4, and 0.8 of the maximum intensity, which is 8.5 Jy beam⁻¹. The central blue contours are 0.88 mm continuum data in steps of 5σ and 40σ , where $\sigma=5\times10^{-4}$ Jy beam⁻¹. The continuum data mark the position of the VLA 1623A circumbinary disk and VLA 1623B.

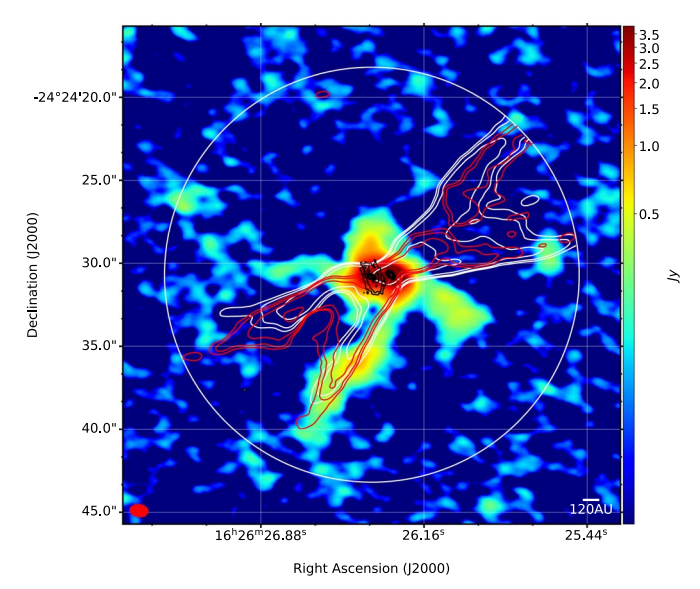


Figure 13. Intensity map of ALMA Cycle 4 SO ($\nu=0$, $J=8_8-7_7$; colors), ALMA Cycle 6 CO (J=3-2; red and white contours), and 0.88 mm continuum (black contours). The CO contours are in steps of 30σ , 50σ , 100σ , and 300σ , where $\sigma=11$ mJy beam $^{-1}$ for CO. The red contours are redshifted integrated CO emission between 8.80 and 17.1 km s $^{-1}$, and the white contours represent blueshifted integrated CO emission between 5.20 and 8.59 km s $^{-1}$. The red circle marks the beam of the SO data, and the white circle represents the field of view for Band 7 CO observation.

and DCO⁺ (J = 3–2) across VLA 1623A circumbinary disk in Figure 15. The PV cut is aligned along the red line shown in Figure 2. The black SO contours mark the extended high-velocity SO emission on the blueshifted side. It spreads out from -4.00 to 2.00, with the center of the circumbinary disk positioned at 0.00. The spatially extended high-velocity SO on the blueshifted side suggests that there are mild accretion shocks that are likely produced by the interaction between accretion flows I and III and the circumbinary disk. Since the northern SO stream is perpendicular to the outflow direction, the contribution from interaction with an outflow is ruled out. In contrast, the SO on the redshifted part is very spatially

compact and located only in the center of the circumbinary disk. The compact structure of the redshifted SO suggests that there are no violent accretion shocks between the redshifted accretion flow VI and the circumbinary disk around VLA 1623A.

3.9. Outflow Signatures from VLA 1623A and VLA 1623B

In Figure 16, we plot the channel maps of the four largescale blueshifted structures from the dendrogram analysis. In previous sections, based on the CO outflows and SO shocks in Figure 13, we established that structure II is an outflow cavity wall. At the exact same position as structure II in Figure 16, we discovered a similar elongated structure (VIII) at lower velocity (2.953–3.293 km s⁻¹). Structure VIII has the same shape and position as structure II, and it is also on top of both the CO outflow and SO shocked southern stream, suggesting that it is also an outflow cavity wall. The two outflow cavity walls traveling at different velocities provide strong evidence indicating that there are two outflows in the plane of the sky coming from VLA 1623A and VLA 1623B, respectively. The Cycle 0 CO results (Santangelo et al. 2015), which are almost completely filtered out by ALMA, suggest that VLA 1623B is driving a much more compact outflow, and the authors associated the slower large-scale outflows with VLA 1623A.

In contrast, our high-resolution Cycle 6 CO data and the discovery of outflow cavity walls (structures II and VIII) suggest otherwise. There are two outflows overlaid on each other in the plane of the sky. The large-scale outflows come from both VLA 1623A and VLA 1623B, as shown by the two outflow cavity walls at two different velocities. From our Cycle 6 CO data, we found that the outflow from VLA 1623B is more redshifted compared to VLA 1623A; therefore, we associate outflow cavity II with outflows from VLA 1623A and outflow cavity VIII with outflows from VLA 1623B. A multitracer analysis to distinguish between the two outflows will be presented in a future paper.

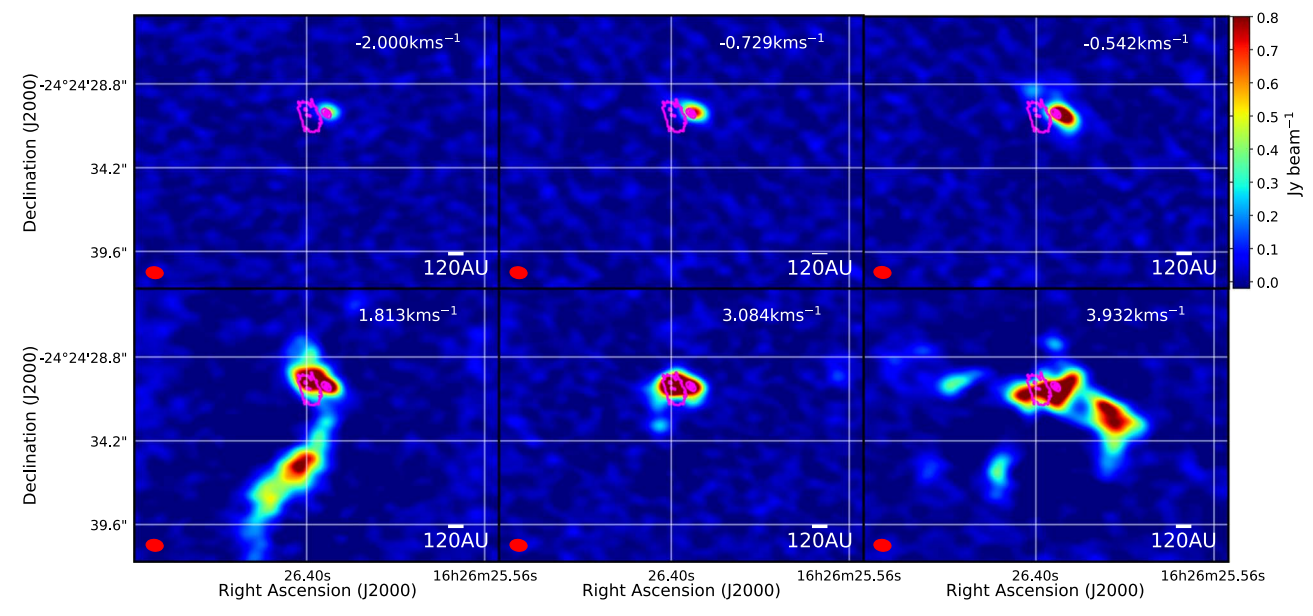


Figure 14. The SO channel maps. The colors represent the ALMA Cycle 4 SO $\nu = 0$, $J = 8_8 - 7_7$ data. The black contours are the 0.88 mm continuum data in steps of 3σ , 5σ , 40σ , and 80σ , where $\sigma = 5 \times 10^{-4}$ Jy beam⁻¹.

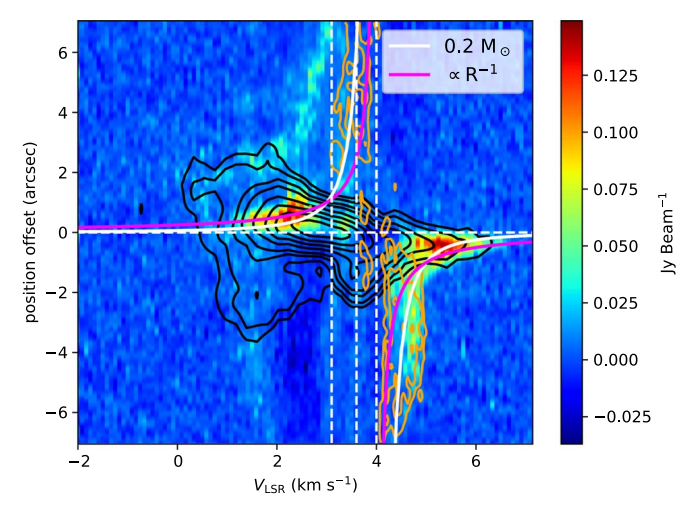


Figure 15. ALMA Cycle 4 SO ($\nu=0$, $J=8_8-7_7$; black contours), ALMA Cycle 2 C¹⁸O with natural weighting (J=2–1; colors), and DCO+ (J=3–2; orange contours) PV diagram on VLA 1623A. The contours are in steps of 5σ , 10σ , 20σ , 30σ , 50σ , 70σ , and 90σ , where $\sigma=15$ and 4.4 mJy beam⁻¹ for SO and DCO+, respectively. The magenta solid line is the infall profile with conserved angular momentum, and the white solid line is the Keplerian rotation profile with a central stellar mass of $0.2~M_{\odot}$ and an inclination angle of 55° .

3.10. Existence of Wall-like Structure South of VLA 1623B

The PV diagrams of SO ($J=8_8-7_7$), $C^{18}O$ (J=2-1), and DCO⁺ (J=3-2) on VLA 1623B, centered at α (J2000) = $16^{\rm h}26^{\rm m}26^{\rm s}305$, δ (J2000) = $-24^{\circ}24'30''.705$ with a position angle of 222°.8, are plotted in Figure 17. In the blueshifted region at the position offset around 3".0, we observed a similar extended high-velocity blueshifted SO feature (compare to Figure 15), which corresponds to the shock fronts of accretion flows I and III. The SO emission has a very wide line width (>10 km s⁻¹) at the position offset of ± 1 ."0 (across VLA 1623B). The huge velocity dispersion on VLA 1623B indicates that there is a huge change in velocity on VLA 1623B, and huge shock fronts are formed. Furthermore, to the south of VLA 1623B, the materials only have a velocity around 4.0 km s⁻¹, suggesting that the SO is at rest. The huge change in

SO velocity and materials (C¹⁸O, SO, DCO⁺) to the south of VLA 1623B at rest suggests that a wall-like structure is located south of VLA 1623B.

In the previous section, the redshifted accretion flow VI is identified to be connected to VLA 1623B (see Figures 6 and 8 and). When the materials from the blueshifted accretion flow III accrete onto VLA 1623B, they are quickly stopped by the redshifted accretion flow VI (shown in Figure 8). The collision between the blueshifted accretion flow III and redshifted accretion flow VI on VLA 1623B slows down the materials and forms an extended wall-like structure south of VLA 1623B. This explains why no violent accretion shocks from the redshifted accretion flow VI are observed around the VLA 1623A circumbinary disk. The redshifted accretion flow VI is already significantly slowed down around VLA 1623B.

To constrain the size of the wall-like structure south of VLA 1623B, we analyze the SO PV diagram in Figure 17. In Figure 17, around a systematic velocity of 4 km s⁻¹, there exists a long extended SO and DCO⁺ on the south (negative offset) side of VLA 1623B. Here DCO⁺ would have an abundance enhancement when the temperature is below the CO freeze-out temperature (Mathews et al. 2013). However, DCO⁺ emission at rest around the disk is contaminated from the envelope, making it not ideal to trace the wall-like structure south of the circumbinary disk. On the other hand, SO, which has high sublimation temperature of 50 K, traces the shock region near the centrifugal barrier (Sakai et al. 2014). The SO in Figure 17 extends to around 6.75 (~780 au). Therefore, the wall on the south side of VLA 1623B has a plane-of-sky width of at least 780 au.

4. Discussions

4.1. Explanations of the Super-Keplerian Rotation in the Inner Region of the Disk

As discussed in Section 3.2, we identified a blueshifted (super-Keplerian) rotation region between 1.5 and 2.0 $\,\rm km\,s^{-1}$ within 1.0 in position offset. A clear gap between the VLA 1623A circumbinary disk and the blueshifted accretion flow I

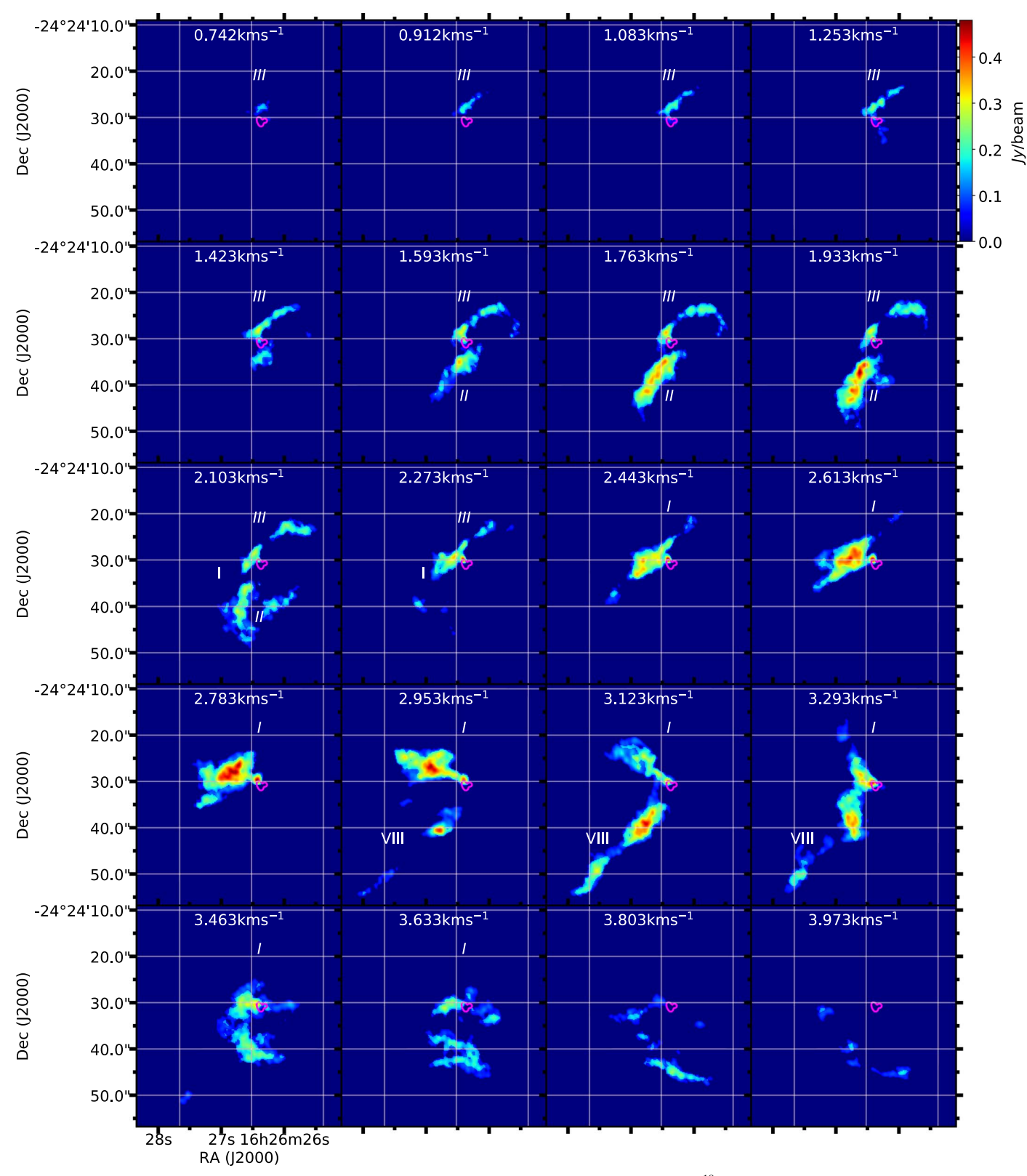


Figure 16. The VLA 1623A and blueshifted structure I, II, III, and VIII channel maps. The colors represent the $C^{18}OJ = 2-1$ (Briggs -1.5) emission identified by the dendrogram algorithm. The magenta contours are 0.88 mm continuum data. The contours are in steps of 5σ , where $\sigma = 5 \times 10^{-4}$ Jy beam⁻¹.

can be found between 2.3 and $3.2 \,\mathrm{km \, s^{-1}}$ in Figure 7, as well as the PV diagram in Figure 4(a) (marked by a white arrow). This gap sets a clear boundary between the blueshifted accretion flow I and the disk. This further rules out the possibility that the blueshifted super-Keplerian rotation region is part of any

large-scale structure or accretion flow in the line of sight, as the disk and accretion flow I are clearly separated in position and velocity space by a gap, as shown in Figure 4(a). The fact that the magenta infall velocity profile passes through the inner region of the disk but deviates significantly on the outer edge of

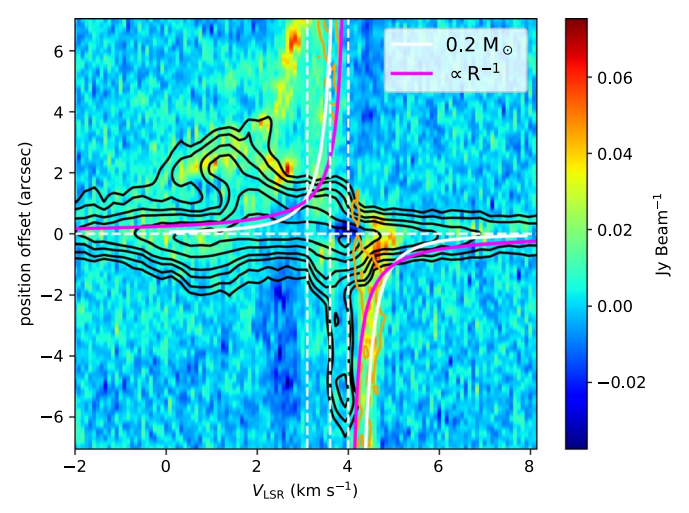


Figure 17. ALMA Cycle 4 SO ($\nu=0$, $J=8_8-7_7$; black contours), ALMA Cycle 2 C¹⁸O with natural weighting (J=2–1; colors), and DCO+ (J=3–2; orange contours) PV diagram on VLA 1623B. The contours are in steps of 5σ , 10σ , 20σ , 30σ , 50σ , 70σ , and 90σ , where $\sigma=15$ and 8 mJy beam⁻¹ for SO and DCO+, respectively. The magenta solid line is the infall profile with conserved angular momentum, and the white solid line is the Keplerian rotation profile with a central stellar mass of $0.2~M_{\odot}$ and an inclination angle of 55° . Note that the central velocity of SO is shifted to $3~{\rm km~s}^{-1}$.

the circumbinary disk on the redshift side suggests that this high-velocity super-Keplerian region inside the disk has different angular momentum from the large-scale accretion flows. Thus, an important question remaining to be answered is whether or not the high-velocity blueshifted component (super-Keplerian rotation region) is part of the disk structure.

One possible explanation for this super-Keplerian rotation region is disk flaring. For a flared disk, due to the *z*-direction projection effect, it is possible that the inner region of the disk is projected to positions further away from the disk center. To take into account the disk flaring and projection effects, we developed a more sophisticated 3D flared disk model to model the observation data. By comparing the model with the ALMA data, we tested this interpretation.

As shown in Figure 20, all of the flared disk models (thick black contours) cannot explain the blueshifted super-Keplerian rotation region in 0."5 position offset at a velocity range of $1.5-2.0 \text{ km s}^{-1}$. The mismatch between the flared disk model and the data shows that the super-Keplerian rotation region is not due to the projection effects of a flared disk. If the super-Keplerian region is due to projection effects, one would expect the disk to be very flared, so the higher-velocity materials in the inner region can be projected at larger position offsets. In Figure 9, at 1.5 km s⁻¹, the white Keplerian rotation line has a position offset of 0".2 (\sim 24 au) lower than the C¹⁸O data, which locates at 0".5-0".7 (60-80 au). Considering an inclination of 55°, if the super-Keplerian rotation region is due to projection effects, then one would expect that the majority of the C¹⁸O is distributed around 40–70 au above the disk plane. To achieve this, the scale height of the disk, the location where the density drops to a fraction of 1/e from the midplane, must be much greater than 40 au. Our flared disk models constrained the disk scale height to be within 15 au, thus showing that this super-Keplerian rotation region is not due to projection effects from a flared disk.

The flat and flared Keplerian disk modeling cannot explain the high-velocity super-Keplerian rotation region in the inner part of the disk. Previous dendrogram analyses found a gap between the accretion flows and the circumbinary disk, suggesting that this super-Keplerian rotation region is not coming from large-scale accretion flows in the line of sight. It is within 180 au of the circumbinary disk. There are two possible explanations for this super-Keplerian rotation region. (i) It is due to collision with infalling materials from the envelope. The materials from above the circumbinary disk plane fall onto the inner region of the circumbinary disk. The collision results in the net gain of angular momentum in the inner region of the disk. (ii) Previous Cycle 0 data underestimated the mass; the combined mass of the binary should be $0.3-0.5\ M_{\odot}$ instead of $0.2\ M_{\odot}$.

The collision between the circumbinary disk and the infalling materials from above the disk plane can provide enough acceleration to explain the super-Keplerian rotation region. Previously, we have used the dendrogram to identify large-scale accretion flows. We found a 120 au wide gap between accretion flow I and the circumbinary disk. In order to create a high-velocity C¹⁸O component only in the inner region of the circumbinary disk, the infalling materials can only collide with the circumbinary disk from above the disk plane. Moreover, with outflows perpendicular to the disk, the allowed infalling angles lie only between the outflow and the disk. Note that one important feature of the super-Keplerian region is that it is symmetric in both blueshifted and redshifted regions. Consider the materials moving in a 60 au circular orbit with a circular velocity on the order of $\sim 2 \text{ km s}^{-1}$; the timescale to complete one orbit is on the order of \sim 200 yr. This timescale is significantly smaller than the disk evolution time scales. We expect any asymmetry features caused by the infalling materials onto the disk to be smoothed out, creating a symmetric feature on both the blueshifted and redshifted sides of the PV diagram. The short orbital period compared to the outer disk evolution timescales ($\sim 10^4$ yr) also implies that any infalling signatures are only transient structures, making them unlikely to be observed if the infalling materials are not continuously supplied by the envelope.

Another possible explanation of the inner super-Keplerian region is a higher combined binary mass. This would mean that the previous mass estimate $(0.2~M_{\odot})$ from Cycle 0 (Murillo et al. 2013) underestimates the mass. To check this possibility, we plot the escape velocities as dotted lines for both combined binary masses of 0.2 and 0.5 M_{\odot} in Figure 18.

The upper left stream (blueshifted accretion flow I, marked by the red arrow) appears to match the escape velocity for $0.5\,M_\odot$. Infalling streams must have a velocity less than the escape velocity. Thus, the sum of the surrounding envelope mass and combined binary mass must be greater than $0.5\,M_\odot$. Since a class 0 protostar is still deeply embedded in the envelope (Seifried et al. 2015), and the envelope mass could be comparable to or larger than the central star, the motion of accretion flows cannot completely break the degeneracy in combined binary mass.

Unlike the case with a combined binary mass of $0.2~M_{\odot}$ (Murillo et al. 2013; white solid line Figure 18), the Keplerian rotation line for a combined binary mass of $0.5~M_{\odot}$ (magenta solid line in Figure 18) passes through the high-velocity blueshifted component perfectly. It will, however, need the circumbinary disk to be asymmetric in the outer region. For the magenta solid lines, the blueshifted disk between 1.0 and 2.0 rotates faster than the Keplerian rotation, while at the same position, the redshifted disk is sub-Keplerian (marked by white

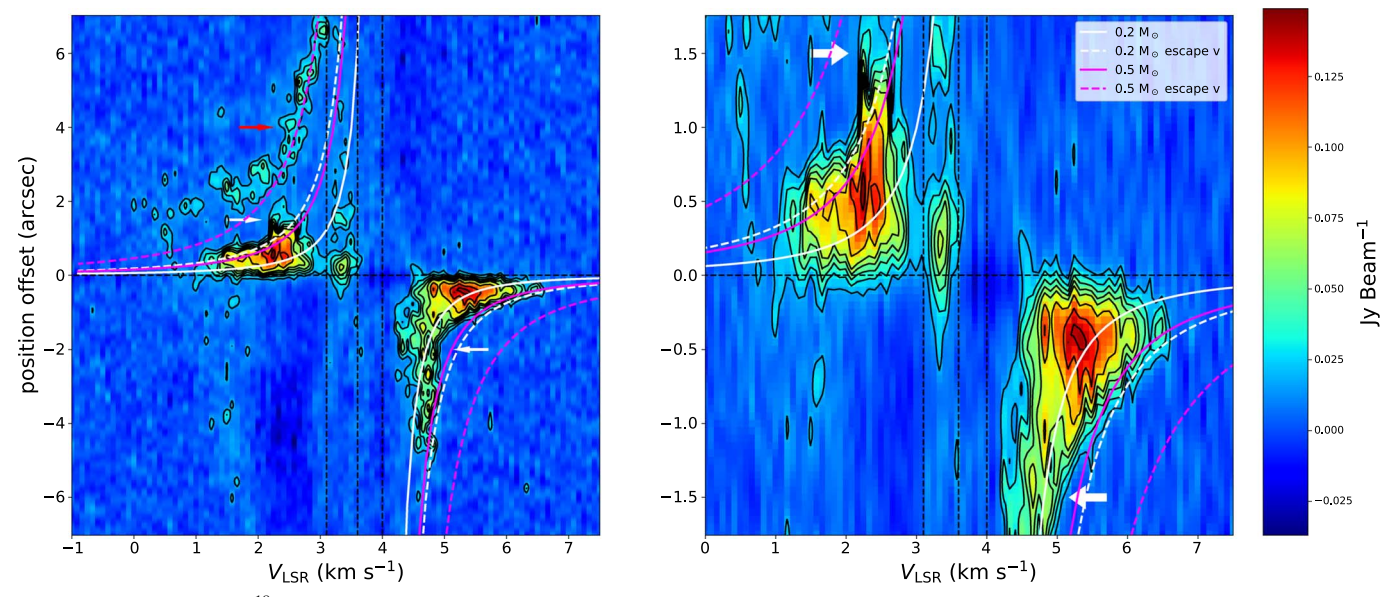


Figure 18. (a) PV cut of the $C^{18}O$ J=2-1 ALMA Cycle 2 VLA 1623A Keplerian disk (natural weighting), centered at VLA 1623A with a position angle of 209°82. The white and magenta solid lines represent the Keplerian rotation profile with a central mass of 0.2 and 0.5 M_{\odot} , respectively. The inclination angle is set to be 55°. The dotted lines mark the corresponding escape velocities. The white arrow marks the position of the Keplerian disk that is asymmetric in motion. The red arrow marks the blueshifted accretion flow I. The black vertical lines mark the velocities of the major large-scale emission. (b) Zoomed-in image of panel (a).

arrows). The observation of blueshifted SO shocks north of the disk might be a possible explanation of this asymmetry in motion.

To break the mass degeneracy, we fit the PV diagram across VLA 1623A with a careful treatment. First, we mask out all pixels with negative flux. Then, for each velocity channel, we search for the peaks above 3σ at different positions. This will allow us to identify different structures at each velocity channel. Then, we remove the infalling stream (red arrow in Figure 18) and use the data that are at least $0.5 \, \mathrm{km \, s^{-1}}$ away from the systematic velocity $(4.0 \, \mathrm{km \, s^{-1}})$ to prevent contamination. An intensity-weighted position average is then calculated to determine the representative disk position for each velocity channel. The nonlinear least-squares fitting result yields a central binary mass of $0.3 \, M_{\odot}$. If one assumes that all gas should be sub-Keplerian in the disk and the Keplerian rotation line should "match only the edge of the PV diagram," then a mass of $0.5 \, M_{\odot}$ would be obtained.

From the flat and flared disk modeling to the infalling streams from accretion flow I, we have concluded that the most plausible explanation of super-Keplerian motion is the underestimation of the combined binary mass of VLA 1623A. The combined binary mass of VLA 1623A should be $0.3-0.5\,M_{\odot}$.

4.2. Summarized Picture

The results of flat and flared disk modeling show that the VLA 1623A circumbinary disk is a large, flat Keplerian disk with a size of 180 au and a combined binary mass of $0.3-0.5\,M_\odot$. At the edge of the circumbinary disk, it is estimated to have a thickness around 30 au based on CMU modeling, which shows that the thickness of the incoming accretion flows at the centrifugal radius is around 30 au (P.-I. Cheong et al. 2020, in preparation).

In the previous sections, we used both SO $J=8_8-7_7$ and C¹⁸O J=2-1 data to study how the accretion flows interact with the circumbinary disk around VLA 1623A and VLA 1623B. A cartoon diagram of their interactions is summarized

in Figure 19 for a combined binary mass of $0.5 M_{\odot}$. In short, there are around three main accretion flows found in this study: blueshifted accretion flows I and III and redshifted accretion flow VI, as summarized in Table 3.

From the extended emission in the SO PV diagram (Figure 15), we identified an accretion shock north of the circumbinary disk around VLA 1623A. This SO accretion shock is produced by the blueshifted accretion flows I and III colliding with the edge of the circumbinary disk. The blueshifted accretion flow III also collides with the redshifted accretion flow VI on VLA 1623B (Figure 16). The collision creates an extremely wide SO line width (>10 km s⁻¹) corresponding to the violent shocks on VLA 1623B. The collision significantly slows down and stops the materials from the redshifted accretion flow VI at a position south of VLA 1623B, forming a wall-like structure as shown in Figure 16.

The materials from the redshifted accretion flow VI continue to pile up, spread to the south of the VLA 1623A circumbinary disk, and infall toward it. The infall of rotating materials is connected to the boundary of the disk and extended up to $\sim\!500\,\mathrm{au}$ south of the circumbinary disk. This explains the extended redshifted C¹8O emission in Figure 3. Furthermore, the outflow collides with this infall of rotating materials and forms a long extended SO southern stream in Figure 13 with a peak located around 4.0 south of the disk. The overall picture of the interactions between accretion flows and circumbinary disks around VLA 1623A and VLA 1623B is summarized in Figure 19.

4.3. SO North of the VLA 1623A Circumbinary Disk and VLA 1623B: Shocks or Infall/Rotation?

The SO north of the disk and VLA 1623B in Figures 15 and 16 (more positive positional offsets) appears to have a similar line width as compared to C¹⁸O, which traces infall and rotation. However, the SO north of the VLA 1623A circumbinary disk and VLA 1623B is actually tracing a mild shock instead of infall and rotation. In the higher 0."3 resolution

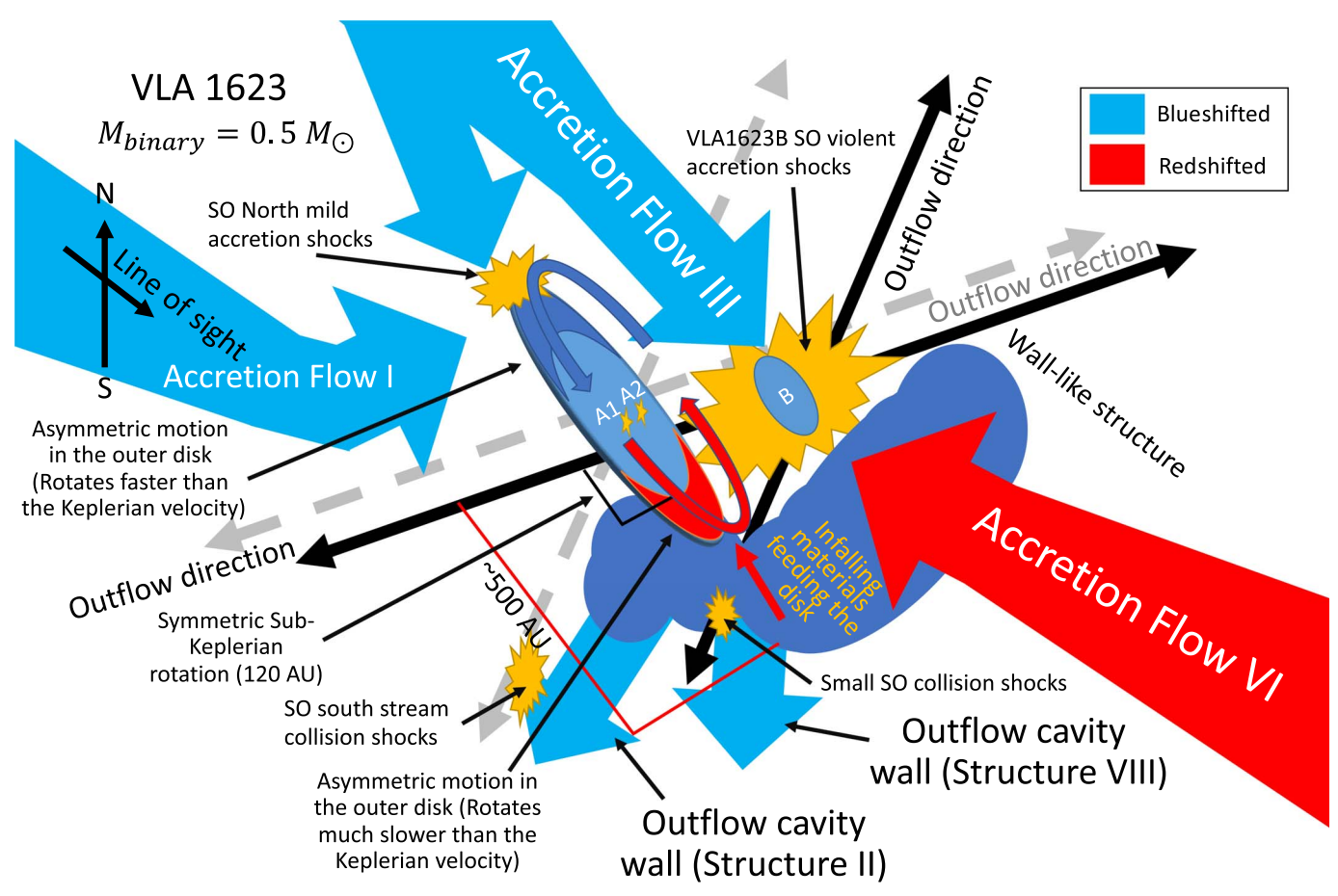


Figure 19. Cartoon diagram of accretion flows and disk interactions studied in this work toward the VLA 1623A circumbinary disk and VLA 1623B for a combined VLA 1623A binary mass of $0.5 \, M_{\odot}$.

SO 3Σ $\nu=0$ 7(8)–6(7) observation (project code: 2018.1.00388.S; PI: Cheng-Han Hsieh), two compact SO peaks are observed north of VLA 1623A and VLA 1623B (C.-H. Hsieh et al. 2020, in preparation). The SO line widths of those peaks are 4 and $7~{\rm km\,s}^{-1}$, which is significantly larger than the C¹⁸O line width (C.-H. Hsieh et al. 2020, in preparation), suggesting that they very likely originated from a shock. A more in-depth study of shocks around the VLA 1623 system will be presented in a future paper.

5. Conclusions

This work presents a detailed analysis of the VLA 1623A circumbinary disk and VLA 1623B. The results can be summarized as follows.

- 1. The super-Keplerian rotation region inside the VLA 1623A circumbinary disk cannot be fitted properly with either flat or flared Keplerian disk models with a binary mass of $0.2\,M_\odot$. This is due to the results of the Cycle 0 data significantly underestimating the binary mass. Based on accretion streams (Figure 18) and disk modeling, we suggest that the combined binary mass for VLA 1623A should be $0.3-0.5\,M_\odot$.
- From the SO PV diagrams, we detect the existence of a wall-like structure south of VLA 1623B. The wall has a plane-of-sky width of around 780 au on the VLA 1623B side. Furthermore, plausible pictures of how accretion

- flows interact with the VLA 1623A circumbinary disk and VLA 1623B are constructed and shown in Figure 19.
- 3. From the dendrogram analysis, we discovered two outflow cavity walls (structures II and VIII) at the same position moving at different velocities. This is strong evidence suggesting that there are two large-scale CO outflows in the plane of the sky on top of each other originating from VLA 1623A and VLA 1623B.

C.H.H. and S.P.L. acknowledge support from the Ministry of Science and Technology of Taiwan with grant MOST 106-2119-M-007-021-MY3. Z.Y.L. is supported in part by NASA grants 80NSSC18K1095 and NNX14B38G and NSF grants AST-1815784, 1910106, and 1716259. The authors further thank Héctor Arce, Paolo Coppi, and the referee for helpful discussions and/or commenting on drafts of this manuscript. This paper makes use of the following ALMA data: ADS/JAO. ALMA #2011.0.00902.S, #2013.1.01004S, #2015.1.00084S, #2016.1.01468, #2018.1.00388.S. ALMA is a partnership of the ESO (representing its member states), NSF (USA), and NINS (Japan), together with the NRC (Canada), NSC and ASIAA (Taiwan), and KASI (Republic of Korea), in cooperation with the Republic of Chile. The Joint ALMA Observatory is operated by the ESO, AUI/NRAO, and NAOJ. The National Radio Astronomy Observatory is a facility of the National Science Foundation operated under cooperative agreement by Associated Universities, Inc.

Software: RADMC-3D (Dullemond et al. 2012), GLUE (Beaumont et al. 2014), CASA (McMullin et al. 2007), astropy (The Astropy Collaboration 2018).

Appendix A Estimation of Centrifugal Radius

Consider a simple disk such that the gravitational acceleration balances the centrifugal force, where j is the specific angular momentum:

$$\frac{GM_*}{r^2} = \frac{j^2}{r^3}. (8)$$

The centrifugal radius r_c can be expressed in terms of the specific angular momentum (j) as follows:

$$r_c = \frac{j^2}{GM_*}. (9)$$

If the disk is in hydrostatic equilibrium in the vertical direction (z), the total column density (σ) can be expressed in terms of the volume density at the midplane (ρ_c) as

$$\sigma = \sqrt{\frac{2c_s^2 \rho_c}{\pi G}},\tag{10}$$

where c_s is the sound speed. It is simple to show that

$$\frac{c_s j}{GM_*} = \frac{c_s \omega_c r^2}{G \sigma \pi r^2} = \frac{\omega_c}{\sqrt{2\pi G \rho_c}}.$$
 (11)

Numerical simulations by Matsumoto et al. (1997) have shown the factor

$$\frac{\omega_c}{\sqrt{2\pi G \rho_c}} \approx 0.3. \tag{12}$$

Therefore, the centrifugal radius¹¹ can be expressed as

$$r_c = \frac{j^2}{GM_*} = \frac{GM_*}{c_s^2} \left(\frac{c_s j}{GM_*}\right)^2 \approx 0.09 \frac{GM_*}{c_s^2}.$$
 (13)

Using the sound speed relation

$$c_s^2 = \frac{k_{\rm B}T}{\mu m_{\rm p}},\tag{14}$$

where $\mu \approx 2.3$, and considering a typical disk temperature of 30 K and a combined binary mass of $0.2\,M_\odot$, we found that the sound speed $c_s\approx 0.33\,\mathrm{km\,s^{-1}}$, and the corresponding centrifugal radius is $\sim\!148\,\mathrm{au}$. For simplicity, the centrifugal radius is close to $\sim\!120\,\mathrm{au}$, so we set the crossover point of constant angular momentum with the Keplerian curve to 1."0 in position offset, which corresponds to a specific angular momentum of 120 au km s⁻¹.

Appendix B Flared Disk Modeling Results

Figure 20 displays the results of the flared disk modeling (zoomed-in image shown in Figure 10)

¹¹ This expression is modified from the star formation lecture notes by Kohji Tomisaka (2007), http://th.nao.ac.jp/MEMBER/tomisaka/Lecture_Notes/StarFormation/3/node85.html.

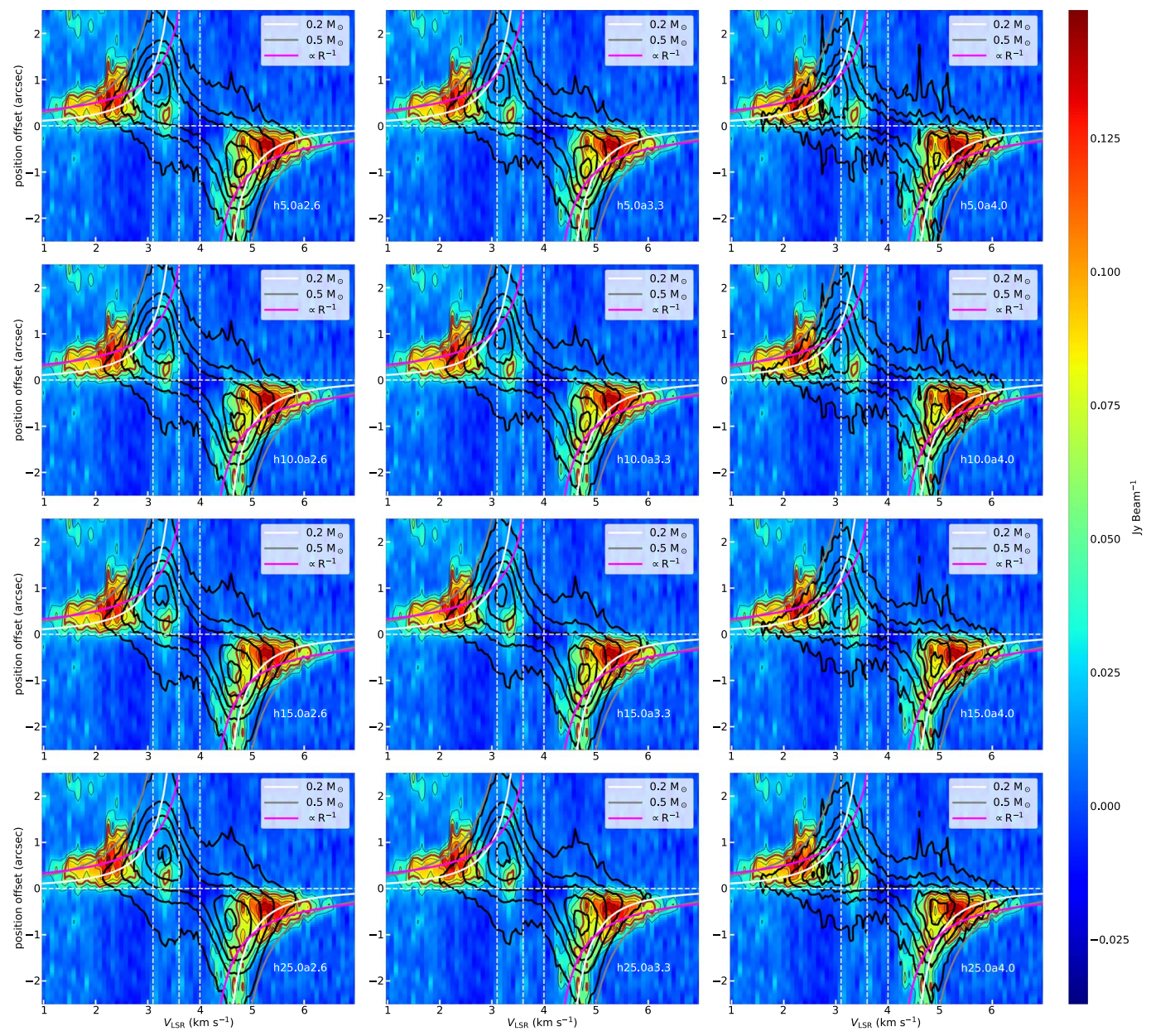


Figure 20. The PV diagrams of the VLA 1623A Keplerian disk overlaid with flared disk model contours with different vertical scale heights h_0 and density power laws a. The colors represent the PV diagram of $C^{18}O$ J=2-1 emission centered at VLA 1623A, and the thin black contours are plotted for 3σ , 5σ , 7σ , 9σ , 11σ , 13σ , and 15σ with $\sigma=9$ mJy beam⁻¹. The thick black contours are from the flared Keplerian disk model with a central binary mass of $0.2~M_{\odot}$. The contours are in steps of 0.2, 0.4, 0.6, 0.8, and 0.95 of the maximum flux in the model. The brown contour marks the 7σ line used for model comparison. The white and gray solid lines represent the Keplerian rotation curve with central star masses of 0.2 and $0.5~M_{\odot}$ and an inclination angle of 55° . The magenta line represents the infall velocity profile with conserved angular momentum. The vertical white lines mark the velocity of the major large-scale emission.

ORCID iDs

Cheng-Han Hsieh https://orcid.org/0000-0003-2803-6358 Shih-Ping Lai https://orcid.org/0000-0001-5522-486X Chia-Lin Ko https://orcid.org/0000-0003-2158-8141

References

Andre, P., Martin-Pintado, J., Despois, D., et al. 1990, A&A, 236, 180
Andre, P., Ward-Thompson, D., & Barsony, M. 1993, ApJ, 406, 122
Aso, Y., Ohashi, N., Aikawa, Y., et al. 2017, ApJ, 849, 56
Beaumont, C., Robitaille, T., & Borkin, M. 2014, Glue: Linked Data Visualizations Across Multiple Files v0.14.2, Astrophysics Source Code Library, ascl:1402.002
Boss, A. P., & Keiser, S. A. 2014, ApJ, 794, 44
Burkert, A., & Bodenheimer, P. 1993, MNRAS, 264, 798

Cassen, P., & Moosman, A. 1981, Icar, 48, 353 Chen, X., Arce, H. G., Zhang, Q., et al. 2013, ApJ, 768, 110 Chiang, E. I., & Goldreich, P. 1997, ApJ, 490, 368 Chou, T.-L., Takakuwa, S., Yen, H.-W., et al. 2014, ApJ, 796, 70 Connelley, M. S., Reipurth, B., & Tokunaga, A. T. 2008, AJ, 135, 2526 Dent, W. R. F., Matthews, H. E., & Walther, D. M. 1995, MNRAS, 277, Duchêne, G., Bontemps, S., Bouvier, J., et al. 2007, A&A, 476, 229 Dullemond, C. P., Juhasz, A., Pohl, A., et al. 2012, RADMC-3D: A multipurpose radiative transfer tool v0.41, Astrophysics Source Code Library, ascl:1202.015 Dutrey, A., Di Folco, E., Beck, T., et al. 2016, A&ARV, 24, 5 Dutrey, A., di Folco, E., Guilloteau, S., et al. 2014, Natur, 514, 600 Guilloteau, S., & Dutrey, A. 1998, A&A, 339, 467 Guilloteau, S., Dutrey, A., Piétu, V., et al. 2011, A&A, 529, A105 Harris, R. J., Cox, E. G., Looney, L. W., et al. 2018, ApJ, 861, 91 Hennebelle, P., & Ciardi, A. 2009, A&A, 506, L29

```
Hennebelle, P., Commerçon, B., Chabrier, G., et al. 2016, ApJL, 830, L8
Inutsuka, S.-I., & Miyama, S. M. 1992, ApJ, 388, 392
Lee, C.-F., Li, Z.-Y., Ho, P. T. P., et al. 2017, ApJ, 843, 27
Loinard, L., Torres, R. M., Mioduszewski, A. J., et al. 2008, ApJL, 675, L29
Mathews, G. S., Klaassen, P. D., Juhász, A., et al. 2013, A&A, 557, A132
Matsumoto, T., Hanawa, T., & Nakamura, F. 1997, ApJ, 478, 569
McMullin, J. P., Waters, B., Schiebel, D., Young, W., & Golap, K. 2007, in
   ASP Conf. Ser. 376, Astronomical Data Analysis Software and Systems
   XVI, ed. R. A. Shaw, F. Hill, & D. J. Bell (San Francisco, CA: ASP), 127
Mellon, R. R., & Li, Z.-Y. 2008, ApJ, 681, 1356
Murillo, N. M., & Lai, S.-P. 2013, ApJL, 764, L15
Murillo, N. M., Lai, S.-P., Bruderer, S., et al. 2013, A&A, 560, A103
Murillo, N. M., van Dishoeck, E. F., van der Wiel, M. H. D., et al. 2018, A&A,
Offner, S. S. R., Kratter, K. M., Matzner, C. D., et al. 2010, ApJ, 725, 1485
Ortiz-León, G. N., Loinard, L., Kounkel, M. A., et al. 2017, ApJ, 834, 141
Padoan, P., & Nordlund, A. 2002, ApJ, 576, 870
Pineda, J. E., Offner, S. S. R., Parker, R. J., et al. 2015, Natur, 518, 213
Raghavan, D., McAlister, H. A., Henry, T. J., et al. 2010, ApJS, 190, 1
Sakai, N., Sakai, T., Hirota, T., et al. 2014, Natur, 507, 78
```

```
Sana, H., & Evans, C. J. 2011, in IAU Symp. 272, Active OB Stars: Structure,
  Evolution, Mass Loss, and Critical Limits, ed. C. Neiner et al. (Cambridge:
  Cambridge Univ. Press), 474
Santangelo, G., Murillo, N. M., Nisini, B., et al. 2015, A&A, 581, A91
Santos-Lima, R., de Gouveia Dal Pino, E. M., & Lazarian, A. 2012, ApJ,
Santos-Lima, R., de Gouveia Dal Pino, E. M., & Lazarian, A. 2013, MNRAS,
  429, 3371
Seifried, D., Banerjee, R., Pudritz, R. E., et al. 2015, MNRAS, 446, 2776
Takakuwa, S., Saito, M., Lim, J., et al. 2012, ApJ, 754, 52
Tang, Y.-W., Dutrey, A., Guilloteau, S., et al. 2014, ApJ, 793, 10
Tang, Y.-W., Dutrey, A., Guilloteau, S., et al. 2016, ApJ, 820, 19
The Astropy Collaboration 2018, Astropy v3.0.5: A Core Python Package for
   Astronomy, Zenodo, doi:10.5281/zenodo.1461536
Tobin, J. J., Hartmann, L., Chiang, H.-F., et al. 2013, ApJ, 771, 48
Tobin, J. J., Looney, L. W., Li, Z.-Y., et al. 2016, ApJ, 818, 73
Tomida, K., Okuzumi, S., & Machida, M. N. 2015, ApJ, 801, 117
Ulrich, R. K. 1976, ApJ, 210, 377
```

Yen, H.-W., Takakuwa, S., Ohashi, N., et al. 2014, ApJ, 793, 1

Yu, T., & Chernin, L. M. 1997, ApJL, 479, L63